POLITECNICO DI TORINO

Department of Mechanical and Aerospace Engineering

Master's Degree
in Mechanical Engineering

Master's Degree Thesis

Design of a cycloidal drive for rotary regenerative shock absorber for motorcycle applications

Tutor:
Professor Nicola Amati
Co-Tutor:
Dr. Salvatore Circosta

Candidate:
Charith Amarasekara

December 2021

Contents

Abstract

The purpose of the study was to optimise a cycloidal gearbox which is then used in the application for a rear regenerative shock absorber for motorcycles. The operating principle of the gearbox has been analysed from the point of view of possible configuration layouts and also the analytical equations for static equilibrium, thus providing the optimal design based on several criteria.

Support functions have been written in order to aid in the evaluation of the performance of the gearbox. The functions range from: hertzian pressure acting on the elements within the drive; profile singularity to study the feasibility of the design; and the internal reactions experienced by the elements. The Matlab model is verified against experimental data provided by other similar studies on relevant topics.

Geometrical parameters related to the overall performance were used as free variables for the optimisation, while respecting the geometrical and operational limitations of the simulation. The optimiser used was the pre-written genetic algorithm available on Matlab called "gamultiobj" which was selected due to its capability to handle several variables and minimise two objective functions simultaneously. The function already assesses each population against the linear and non-linear constraints provided in matrix form.

A sensitivity analysis is also carried beforehand to have an idea of the optimisations results and to evaluate the effect of each variable on the machine's performance.

A CAD Model was finally developed incorporating all the optimised parameters, but also all the auxiliary components needed to render a functioning gearbox, futhermore all the above mentioned components have been sized according to their respective standards.

As a further consideration, the proposal of a non-linear model is suggested because based on the experimental data there is a strong link between the imposed output load affects the overall efficiency of the gearbox.

Chapter 1

Acknowledgements

First and foremost I would like to thank my family for giving me the opportunity to make it up to this point in my life and for the encouragement they've offered over my past few years of study.

I would like to mention a special thanks to my classmates, professors, and friends I've met along the way, from the first year at university.

Finally I would like to give a special thank you to Professor Amati and Dr. Circosta for their tutelage and guidance with regards to this thesis and especially for their dedication to this field.

List of Symbols

Description	Symbol	Units
Transmission ratio	τ	-
Number of lobes	z_1	-
Number of teeth in the casing	z_2	-
Base circle radius	R_p	mm
Rotation angle about base circle	θ	$^\circ$
Roller radius	R_r	mm
Rotational angle about generating circle	γ	$^\circ$
Eccentricity	ρ	mm
Generating circle radius	R_g	mm
Profile modification factor	x_{mod}	-
Number of housing rollers	N_{pr}	-
Input shaft rotation angle	ϕ	$^\circ$
Output pin radius circle	R_{po}	mm
Number of output pins	N_{po}	-
Output pin radius	R_{pin}	mm
Housing roller force	F_p	N
Output pin force	F_q	N
Input shaft force	F_{sp}	N
Roller and pin friction force	$F_{s\mu}$	N
Roller friction coefficient	f_p, μ_p	-
Pin friction coefficient	f_q, μ_q	-
Input shaft friction coefficient	μ_{fsp}	-
Input moment	M_{in}	Nm
Theoretical efficiency	η_{theo}	-
Experimental efficiency	η_{exp}	-
Bending moment	M_f	Nm
YZ bending moment	M_{fx}	Nm
XZ bending moment	M_{fy}	Nm

Description	Symbol	Units
Von mises stress equivalent	σ_{Mises}	Nm
Inertia	I_0	mm^4
Resultant bending moment	M_f	Nm
Safety Factor	S_F	-
Yield strength	σ_Y	Nm
Resultant torsional moment	M_t	Nm
Theoretical curvature profile	R_w	mm^{-1}
Correct curvature profile	R_T	mm^{-1}
Parametric curve radius	K	mm
Parametric curve curvature	R_K	mm^{-1}
Output moment	T_{output}	Nm
Input moment	T_{input}	Nm
Input speed	ω_{in}	rad/s

Chapter 2

Introduction

2.1 Regenerative Shock Absorber Review

Regenerative shock absorber systems is a system that converts kinetic energy from the motion of suspension systems in automotive applications into more useful forms such as electrical energy. There are several different mechanism that can by utilised to achieve this goal. As an example these systems can increase the range of electrical and hybrid vehicles, while providing an alternative source for charging the battery for petroleum vehicles, albeit adding another level of complexity in terms of maintenance and design. Regenerative shock absorbers can be broken down into two main types; linear regenerative shock absorbers and rotary regenerative shock absorbers. The main distinction between the two categories, in the former the linear motion in the suspension is sufficient enough to generate electricity, however with rotary systems the linear motion must be converted into a rotary motion in order to produce electricity.

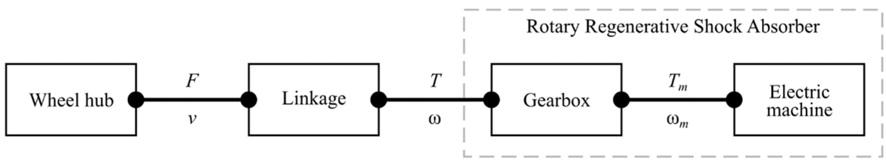

Figure 2.1: Block diagram representing regenerative shock absorbers[1]

Main types of regenerative shock absorbers:

- Planetary
- Harmonic

- Electromagnetic
- Cycloidal

A planetary regenerative shock absorber, which is of the rotary regenerative type and relies on a rack and pinion system like in Figure 2.2. The rack and pinion gear train allows the conversion of the linear motion into a rotary motion, which is then amplified by the planetary gearbox. In all gearboxes of this type the typical carrier is stationary. This gearbox can be utilised both as a regenerative shock absorber, but also as means to tune the damping incorporated into the suspension system by using the regenerative shock absorber in the reverse motion.

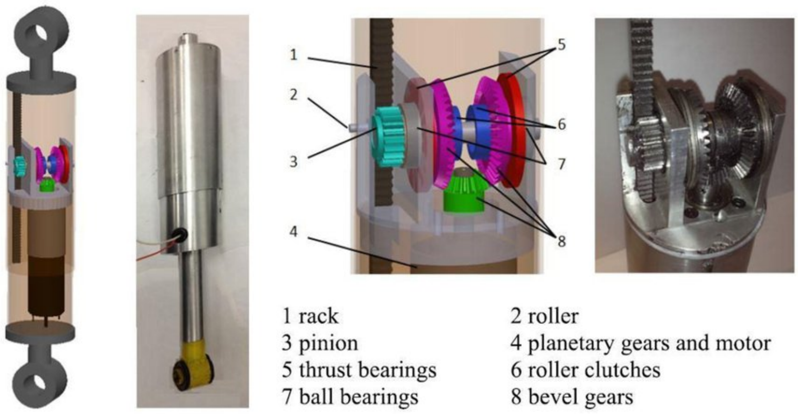

Figure 2.2: Example of planetary regenerative shock absorber[2]

Electromagnetic regenerative shock absorbers are a type of linear regenerative shock absorbers. Figure 2.3 refers to the basic design of an electromagnetic regenerative shock absorber, it relies on the Ampere's law where the relative motion of stator windings through a magnetic field induce a current in the windings. Despite its seemingly simple structure the major drawback regarding this design is the undesirable heat generation due to the eddy currents within the magnets, while one of its more advantages aspects is the lack of contact and therefore longer operating life.

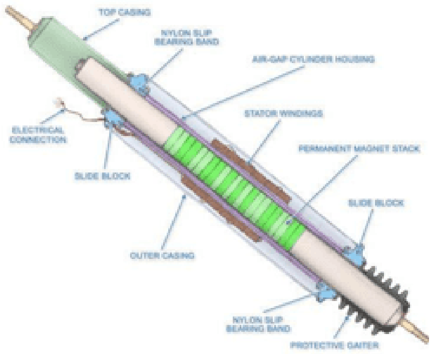

Figure 2.3: Example of electromagnetic regenerative shock absorber[3]

A harmonic gearbox employs an elastic membrane in between the fixed external ring and a smooth inner shaft in the form of an elliptical profile. The profile is connected to either a shaft or a lever. Harmonic gearboxes are a type of rotary regenerative gearbox.

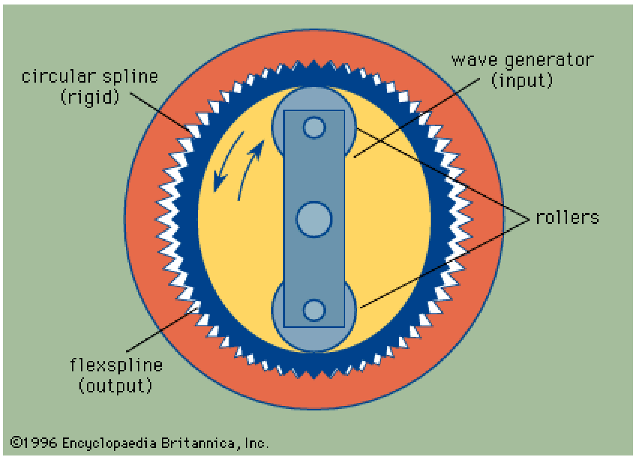

Figure 2.4: Example of harmonic gearbox[4]

Cycloidal gearbox are some of the latest type of regenerative shock absorbers to be developed in the past few decades. These types of rotary regenerative shock absorbers operate on the similar principle to planetary gearbox systems, however while using a cycloidal gearbox to achieve high transmission ratios for relative small packages.

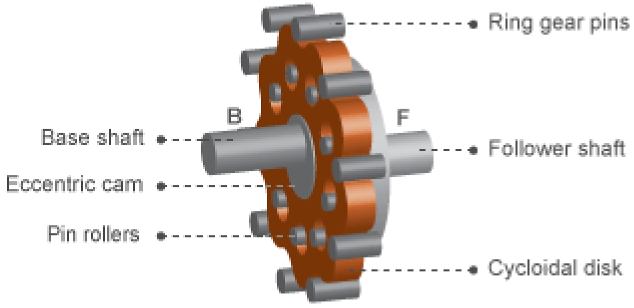

Figure 2.5: Example of cycloidal gearbox[5]

2.2 Thesis Objective

The objective of this thesis is to initially establish a working mathematical model that can simulate the behaviour of a cycloidal gearbox. Once the gearbox model has been established, tuning of the model was carried out by means of experimental data found from other scientific source. The model is accompanied by several supporting functions to evaluate the performance of the gearbox. The model is optimised based on two objective functions and finally a complete cad model is produced containing all necessary auxiliary components for a fully functioning optimised cycloidal gearbox.

2.3 Motorcycle Application

The main purpose of this work was to optimise the cycloidal gearbox found within the rotary regenerative shock absorber. More specifically the gearbox is part of a much bigger system related to motorcycle applications. Basically in motorcycles the rear wheel motion is regulated by means of a suspension system and instead of converting the kinetic energy into a wasteful form of energy it can be harvested therefore a regenerative system to be stored in the form of electrical energy. This objective is achieved by means of a linkage connected to the rear wheel before being attached to the gearbox. The position of the linkage was optimised in a separate optimisation like that seen in Figure 2.7 which was done in this example for a wish bone suspension for auto-mobile applications. The gearbox must respect the physical and operating limitations while been able to fit within the chassis like the example in Figure 2.6.

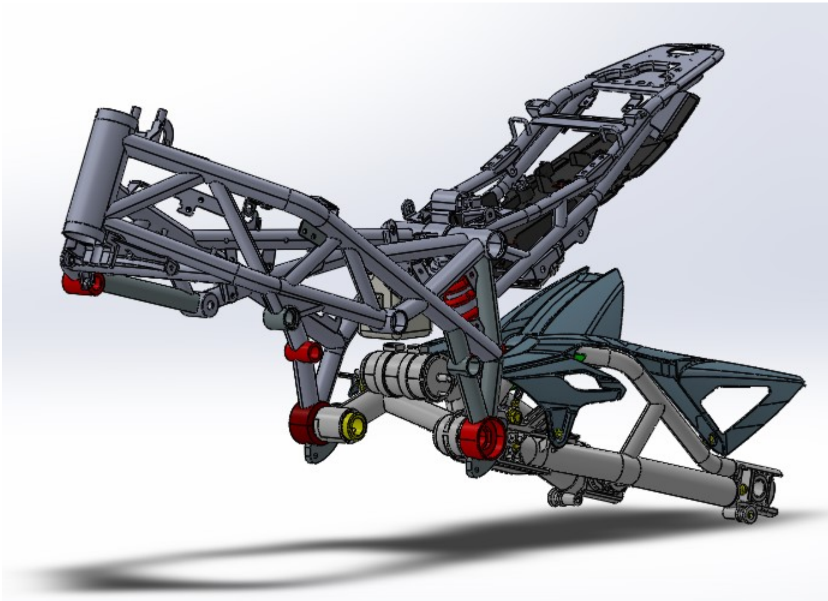

Figure 2.6: Motorcycle chassis with a regenerative shock absorber mounted near the swing arm

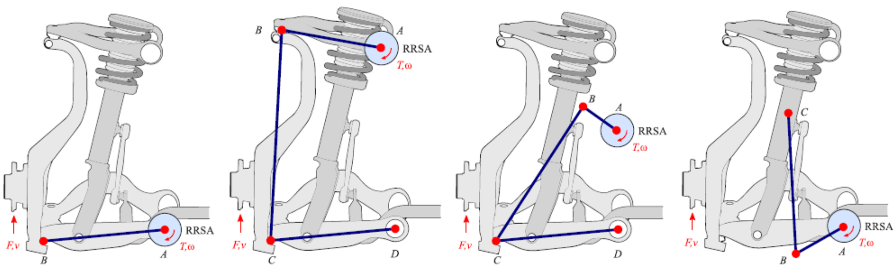

Figure 2.7: Linkage length and position optimisation.[1]

2.4 Thesis Outline

The work has been broken down into sections, namely each section refers to a particular functionality of the drive. The objective of each section is to provide a progressive understanding of the gearbox starting from the basic layout of the principle components within the drive, available both commercially and in scientific papers. The study of the various configurations allows the selection of an appropriate layout that suits the need for this particular application.

After the type of drive configuration is selected the next step was defining the gearbox geometry on the basis of equations and the selected configuration required to construct the geometry of the drive starting from its three main components; cycloidal disk, housing roller positions and output pin positions and holes.

Subsequently using the set of equations defined in the geometry to compute the static equilibrium which is written in the form of two translation equation along the principle x and y directions, followed by the rotational equilibrium along the z axis. In the equilibrium equations the static friction model is introduced by a simple rotation of each respective contact force in the direction to oppose the motion of each component. The static equilibrium enables the calculation of the maximum exchanged forces between the gearbox elements to determine the sinusoidal force distribution amongst each of the roller and pins. Now a working model of a cycloidal drive has been established at this point.

The working model is tuned by taking into account the presence of a static friction model by means of experimental data provided by other scientific sources. The objective is to make the output of the drive in terms of the trend of the efficiency and output torque of the model mimic that of the experimental data within a reasonable interval of confidence.

In addition to the friction model other auxiliary models investigated are; internal reactions within the pins and rollers, hertzian contact between contact forces, and profile singularity.

The hertzian contact involves both convex-concave and concave-concave contact situation where the pressure exerted due to contact forces could cause localized yielding within the material. The calculated stress must be within the admissible stress allowed by the safety factor and yield strength of the material. The opposite is also done by reverse engineering the minimum thickness of the cycloidal disk required and verifying whether default thickness is satisfactory.

The last auxiliary models is to verify the profile of the cycloidal disk for singularities, due to complex shape there could be an issue in terms of feasibility of the disk production which corresponds abrupt changes in the derivatives of the parametric functions. If the abrupt variations of the derivatives are within the pre-prescribed machining tolerances, then singularities can be avoided, which results in a smoother motion of the gearbox.

Another means of quantifying the mass distribution of all the components within the drive is to apply Huygens-Steiner theorem which accounts for the fact that several objects with mass are rotating about an axis that is not the principal axis of rotation.

Before optimising the existing model, a sensitivity analysis is conducted to have an idea of the expected outcome of the optimisation and identify the biggest contributing factors of the overall performance of the gearbox. The analysis is accomplished by the varying one of the many fundamental geometrical parameters and comparing the results against the output of a control set of geometric parameters.

Five geometric parameters influence the drive and are thus considered as the free variables to optimise. Due to the complexity of the optimisation problem a genetic algorithm is proposed to solve the issue. The reason for utilising a genetic algorithm is because of its ability to find a local minima over a wide range domain, however it is not guaranteed to be a global minima. The bounds for each of the free variables are set with accordance of the available physical space. The genetic algorithm generates a population which must satisfy a set of constraints that mainly defines geometrical impossibilities before the simulation is run. The algorithm minimises two objective functions; efficiency and equivalent inertia. The simulation for each population produces a score which is utilized when generating the next population until the end criteria is met, which is either the function tolerance or the maximum number of generations.

Lastly with the optimised variables, a CAD model is developed to facilitate the full functionality of the gearbox, ranging from the bearing type and arrangement to the spacers, seegers and housing case.

Chapter 3

Cycloidal Drive

3.1 Operating Principle

A cycloidal drive is comprised of four parts (shown in Figure 3.1): eccentric shaft, rollers, cycloidal disk, and the output pin shaft. The input torque is transmitted through the eccentric shaft, the eccentricity of the shaft can either be machined onto the end of the shaft or by using an eccentricity cam mounted on a circular shaft.

The cycloidal disk motion is made up of two individual movements: rotation of the disk about the input shaft axis and the rotation of the disk about its own axis. The eccentricity of the shaft causes the first motion while the rollers are responsible for the second motion.

Within the cycloidal disk there are empty circular profiles, where the rollers which are part of the output pin shaft are placed, the coupled motion of the disk tends to push the output pin which are always tangent to the circular profiles while in motion.

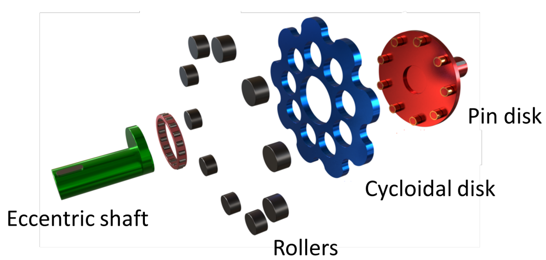

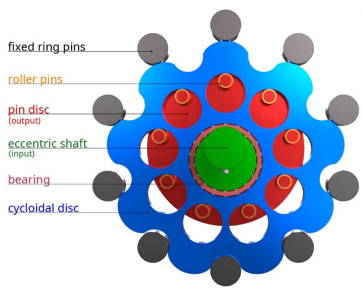

Figure 3.1: Cycloidal gearbox components (left) and top view (right)[6]

The transmission ratio of a cycloidal drive is defined by the Equation 3.1.

Cycloidal drives are able to achieve such high transmission ratio because it takes advantage of the formula for the transmission ratio by minimizing the denominator which implies that the number of housing roller pins must be greater that the number of lobes on the cycloidal disk by the factor of one.

$$\tau = \frac{z_1}{z_1 - z_2} \tag{3.1}$$

3.2 Configuration

Many different configurations of cycloidal drives exist commercially, each configuration serves a particular advantage. Most drives either are constructed using sliding or rotating elements on the surfaces within the drive that are in contact as they tend to produce most of the friction losses. Moreover there are other factors to consider such as:

- Bearing arrangements
- Output shaft shape
- Input shaft shape
- Rollers
- Lobes

Several different types of configurations are currently in service, as seen in the list below, and in the later stages of this section each type of design will discussed and how each of the aforementioned factors will affect their operation.

1. Transcyko: TLB Series
2. Sumitomo: Cyclo 6000 Reducer
3. Eppinger: Cycloidal Gearboxes
4. Nabtesco: RV series
5. Spinea: TwinSpin
6. Scientific Configuration

3.2.1 Transcyko: TLB Series

The first type of cycloidal drive mentioned in Figure 3.2 is the most commonly utilized model due to its high transmission ratio and compact size. The compact size is achieved by instead of using an output shaft but rather an output coupling plate. This type of gearbox is usually comprised of two stages, in addition its housing roller pins are partially embedded within the outer casing to save space. In addition to the second stage which is the cycloidal gearbox, there is also a first stage reduction spur gearbox connected to the input shafts for the second stage cycloidal drive, this type of configuration an exceptionally high overall transmission ratio. The figure below is an example from the Transcyko: TLB Series cycloidal drive.

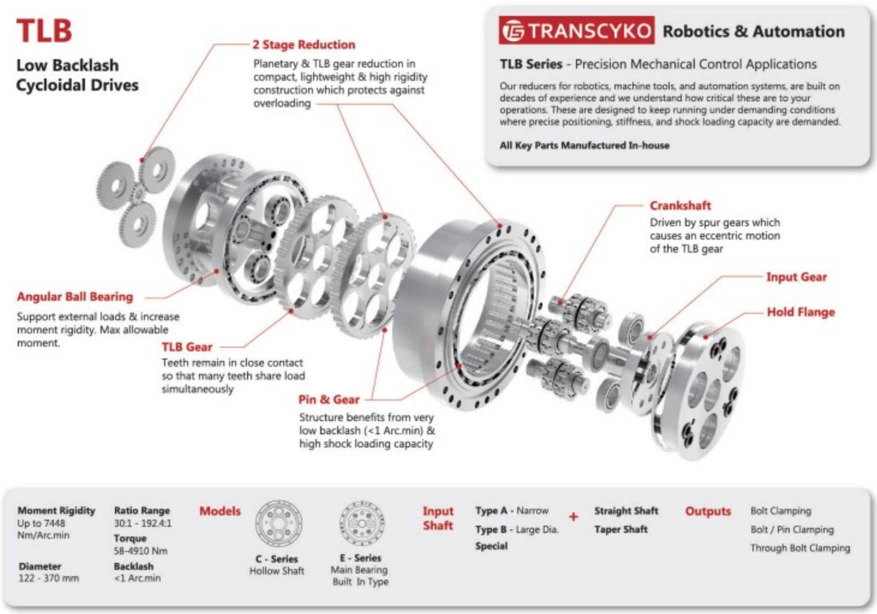

Figure 3.2: TLB Series machine configuration[7]

3.2.2 Sumitomo: Cyclo 6000 Reducer

The second type of commercial drive, shown in Figure 3.3a, is more of a traditional design with respect to its layout. It is much bulkier in terms of size because of the presence of input and output shafts, making it more stable and well equipped to handle not only sudden shocks, but also to sustain much higher loads.

For the sake of simplicity the most suitable model for our purposes is the Sumitomo: Cyclo 6000 reducer. It uses a simple design with sliding sleeves on the rollers and pins to reduce friction losses generated through contact. The positions of the bearing on the output and input shaft offer an adequate support system for the internal reactions of the system.

(a) Cyclo6000 Reducer

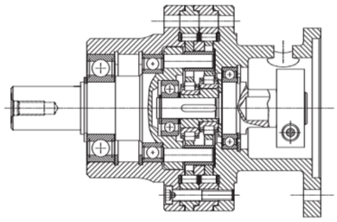

(b) Cyclo6000 Reducer cross section view

Figure 3.3: Cyclo6000 Reducer (right) and its cross section view (left)[8]

3.2.3 Eppinger: Cycloidal Gearboxes

This configuration once again utilises the outer plate as a means of output coupling in an effort to reduce the occupied space by the gearbox. The unique feature of the design the use of an eccentric bearing on the input shaft rather than the tradition solution of utilising an eccentric cam. Using the eccentric bearing offers a longer service life, but increases the complexity of the design.

Figure 3.4: Eppinger machine configuration[9]

3.2.4 Nabtesco: RV series

By far the most technologically advanced solution with not only incorporating some of the features of the previous designs such as the output plate rather than the traditional output shaft. In addition the gearbox has a two stage gear reduction between the input shaft and the cycloidal disk. Instead of a central shaft rotating the disk, the spur gears are connected to the shafts together with eccentric bearings on them to facilitate the disks rotation.

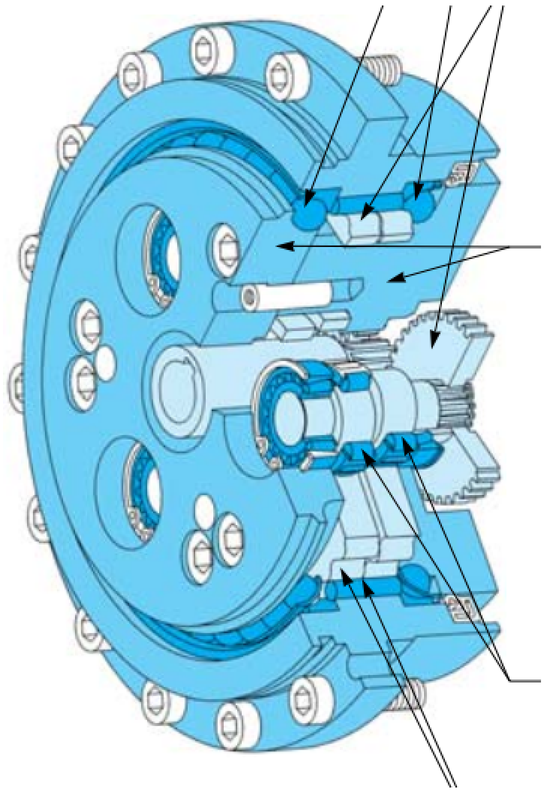

Figure 3.5: Nabtesco machine configuration[10]

3.2.5 Spinea: TwinSpin

Similarly this design uses a straight input shaft with an eccentric bearing, however the special trait regarding this model is that it does not use traditional output pins to cause the rotation of the output shaft, but rather an intermediate plate that pushes the output plate simultaneously in two perpendicular and independent directions to reproduce the circular motion for the output plate.

Figure 3.6: Spinea machine configuration[11]

3.2.6 Scientific Configuration

The most common configuration used for scientific study to analyse behaviour of many different phenomenon such its efficiency, state of stress, and friction modelling just to name a few. The reason behind its suitability for academic study is because of its standard arrangement regarding its traditional output and input shafts followed by the presence of a sturdy bearing configuration for both shafts. Another characteristic that aids a better understanding of this gearbox is that compactness is not its main objective thus all design choices are made in the effort to make the drive function at its best.

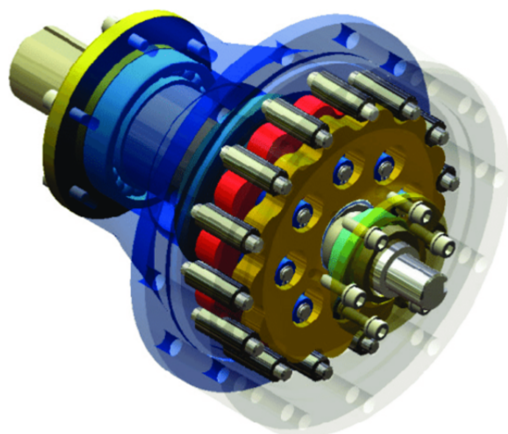

Figure 3.7: Scientific machine configuration[12]

3.3 Geometry

The many advantages of the cycloidal drive are due to the cycloidal disks unique shape, the outline of the cycloidal disk is commonly referred to as the cycloidal profile, it comes from the concept of an epicycloid. An epicycloid is a curve generated by a point on the circumference of a circle that rolls, without sliding, along another circle. The circle to which the point (red point) belongs to is referred to as the generating circle (black circle), while the circle along which the generating circle rolls upon is called the base circle (blue circle), as seen in Figure 3.8.

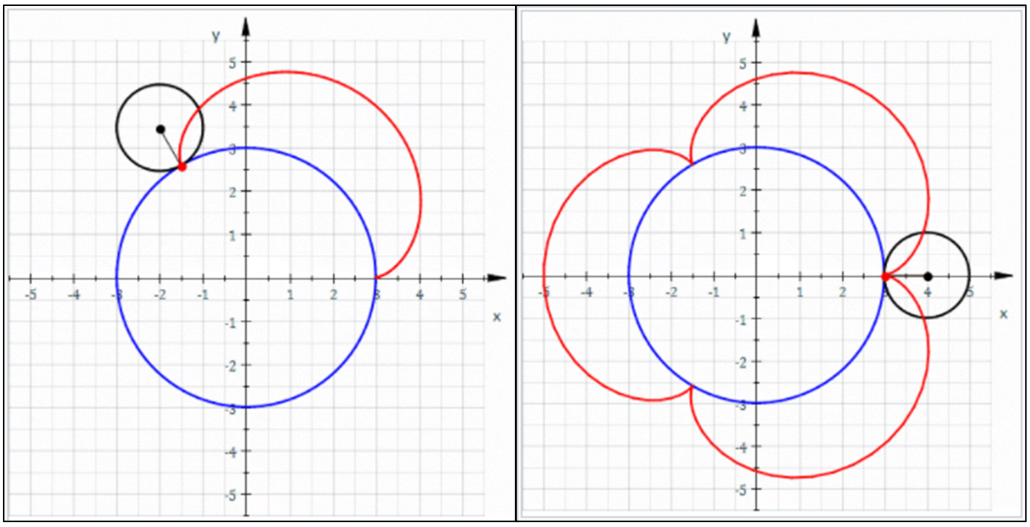

Figure 3.8: Epicycloid curve generation (left) and completed profile (right)

Furthermore there are three types of epicycloid curves:

1. Shortened epicycloid
2. Normal epicycloid
3. Extended epicycloid

Examples of each profile can be seen in Figure 3.9, the shortened profile provides the most practical solution as is present single point of contact between each roller and the disk, while the both the normal and extended profiles have little to no practical value. The shortened or extended profiles can be obtained using an appropriate correction factor that is a proportional to the generation circle.

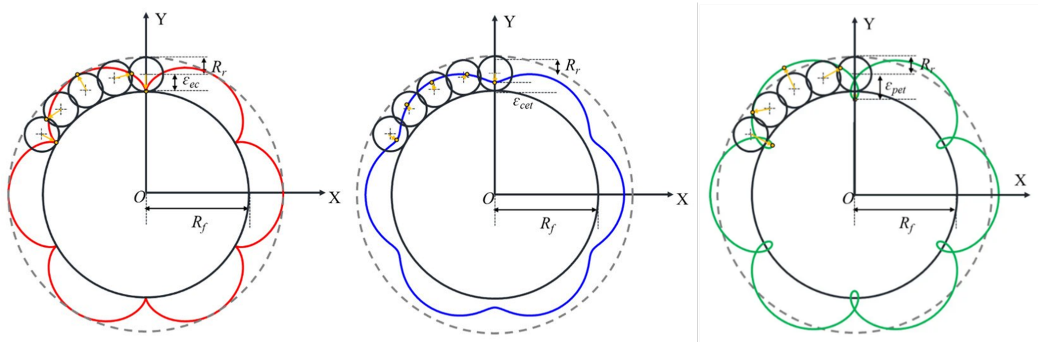

Figure 3.9: Types of epicycloidal profiles[13]

The basic profile of the cycloidal disk is given by the Equation 3.2 and its geometric representation can be seen in Figure 3.10. Complex notation is used due to its ease of handling any algebraic operations. The subscript p of the vector $\left(\overrightarrow{PD}\left(\theta\right)\right)_p$ implies that is drawn with respect to the moving reference frame $(X_P Y_P)$ as shown in Figure 3.10.

$$\left(\overrightarrow{PD}\left(\theta\right)\right)_p = R_p e^{i\theta} + \left(|\overrightarrow{AC}| - R_r\right) e^{i(\theta+\gamma)} \tag{3.2}$$

Where the vector $|\overrightarrow{AC\left(\theta\right)}|$ represents the distance from the profile at point **A** to point **C** which is where the line passing through point **P** (centre of the cycloidal disk) is tangent to the base circle.

$$|\overrightarrow{AC\left(\theta\right)}| = \left({R_g}^2 + \rho^2 - 2R_g\rho\cos\left(\theta\tau\right)\right)^{\frac{1}{2}} \tag{3.3}$$

$$\tau = \frac{R_p}{R_g} \tag{3.4}$$

$$\rho = R_g\left(1 - x_{mod}\right) \tag{3.5}$$

The angle $\gamma\left(\theta\right)$ dictates the angle of the of the vector $\overrightarrow{AC}\left(\theta\right)$ which in other words describes the rotation of the generating circle upon the base circle. The negative sign within the argument of the sinusoidal function is because the positive rotation of θ results in a negative rotation of the generating circle and thus to be consistent the negative sign is required.

$$\gamma\left(\theta\right) = \arctan\left(\frac{\rho\sin\left(-\theta\tau\right)}{R_g - \rho\cos\left(\theta\tau\right)}\right) \tag{3.6}$$

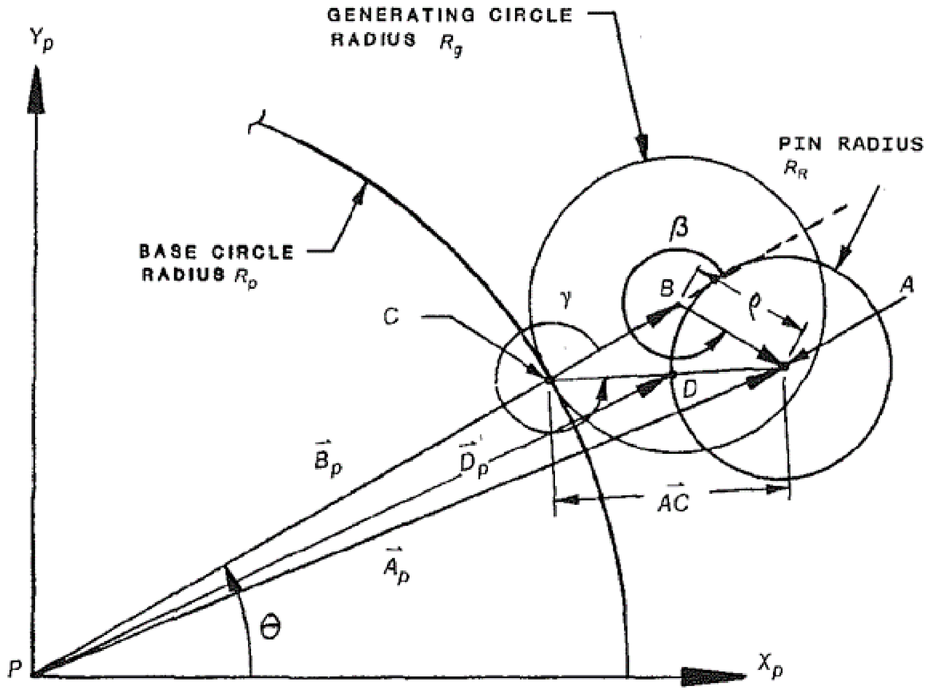

Figure 3.10: Detailed view of epicycloid generation[14]

The housing roller pins lay on the radius of the $\left(\overrightarrow{PA}\left(n_{pr},\theta\right)\right)_p$ vector in Equation 3.7, however there is an angular position for each roller given the Equation 3.8

$$\left(\overrightarrow{PA}\left(n_{pr},\theta\right)\right)_p = \left(R_p + R_g\right)e^{i\theta} - \rho e^{i(\phi(1+\tau))} \tag{3.7}$$

$$\phi\left(\theta, n_{pr}\right) = \theta - \frac{2\pi n_{pr}}{1+\tau} \tag{3.8}$$

Bear in mind that till now all the vectors discussed above were with respect to a moving reference from on the cycloidal disk, however unfortunately the disk is moving about a fixed reference thus an additional vector is required to highlight the motion of the moving reference frame with respect to the fixed reference frame. The fixed reference frame $(X_f Y_f)$ is coincident with the axis of the input shaft.

The **two** movements of the disk can be characterized by the following two vectors:

1. Rotation of the cycloidal disk about fixed frame: $\overrightarrow{OP} = \rho e^{i\psi}$
2. Rotation of the cycloidal disk about its own moving frame: $e^{-i\frac{\psi}{\tau}}$

Therefore for the aforementioned vectors such as that for the trochoidal profile (Equation 3.9) and housing roller center position (Equation 3.10) in terms of the fixed reference will become:

$$\overrightarrow{OD}\,(\theta,\phi) = \left(\left(\overrightarrow{PD}\right)_p e^{-i\frac{\psi}{\tau}}\right) + \overrightarrow{OP} \tag{3.9}$$

$$\overrightarrow{OA}\,(n_{pr},\theta,\phi) = \left(\left(\overrightarrow{PA}\right)_p e^{-i\frac{\psi}{\tau}}\right) + \overrightarrow{OP} \tag{3.10}$$

However the angle value of θ_p required for the Equation 3.10 is based in the following equation: (The subscript p denotes that it is the angle with respect to the moving reference frame)

$$\theta_p\,(n_{pr}) = \frac{2\pi}{N_{pr}}\,(n_{pr}-1) \tag{3.11}$$

Figure 3.11 shows the end results of the shortened epicycloid with the housing roller pins for a given set of parameters provided in the later stages of this work. Notice also the presence of the origins of both the moving (black) and fixed (red) reference frames.

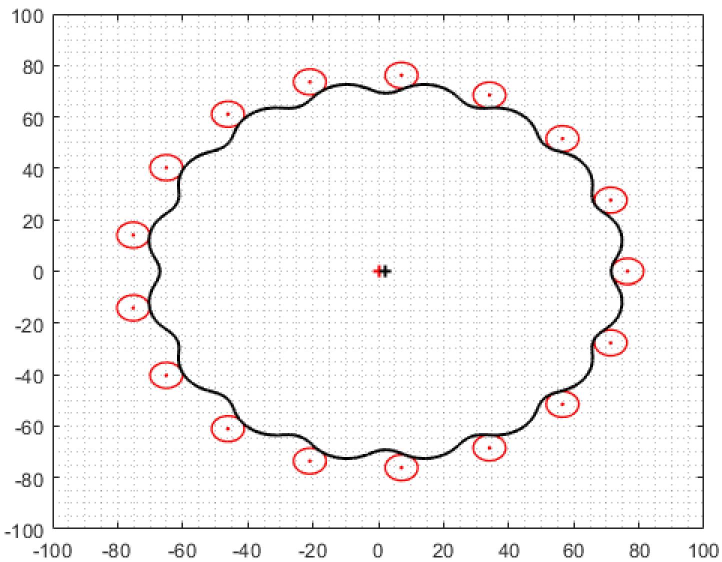

Figure 3.11: Profile after epicycloid generation and housing roller pin positions

The vector $\overrightarrow{AC}\,(n_{pr},\psi)$ can also define the vector along which the force exchanged between the disk and the housing roller is applied. Therefore it can be written in the following form in order to incorporate the other geometrical vectors related to the gearbox rather relying on the its geometrical parameters like in Equation 3.3.

$$\overrightarrow{OC}\left(n_{pr},\psi\right) = R_p e^{i\theta_p} + \overrightarrow{OP}\left(\psi\right) \tag{3.12}$$

$$\overrightarrow{AC}\left(n_{pr},\psi\right) = \overrightarrow{OC}\left(n_{pr},\psi\right) - \overrightarrow{OA}\left(\theta_p, n_{pr}, 0\right) \tag{3.13}$$

The contact point of each lobe with each respective housing roller is given by the vector $\overrightarrow{OD}_{ring}\left(n_{pr},\psi\right)$.

$$\overrightarrow{OD}_{ring}\left(n_{pr},\psi\right) = \overrightarrow{OA}\left(\theta_p, n_{pr}, 0\right) + R_r \frac{\overrightarrow{AC}\left(n_{pr},\psi\right)}{|\overrightarrow{AC}\left(n_{pr},\psi\right)|} \tag{3.14}$$

The ring-pin action line can be parametrized with respect to variable 'a':

$$F_{line}\left(n_{pr},\psi,a\right) = \overrightarrow{OD}_{ring}\left(n_{pr},\psi\right) + a\frac{\overrightarrow{AC}\left(n_{pr},\psi\right)}{|\overrightarrow{AC}\left(n_{pr},\psi\right)|} \tag{3.15}$$

$$[a_i, a_j] = \begin{cases} Re\left(F_{line}\left(n_{pr,i},\psi,a\right) - F_{line}\left(n_{pr,j},\psi,a\right)\right) = 0 \\ Im\left(F_{line}\left(n_{pr,i},\psi,a\right) - F_{line}\left(n_{pr,j},\psi,a\right)\right) = 0 \end{cases} \tag{3.16}$$

The intersection point is therefore given by Equation 3.17 and it can be seen in Figure 3.12 as the green point between each respective F_{line} vector.

$$\overrightarrow{OL} = F_{line}\left(n_{pr},\psi,a\right) \tag{3.17}$$

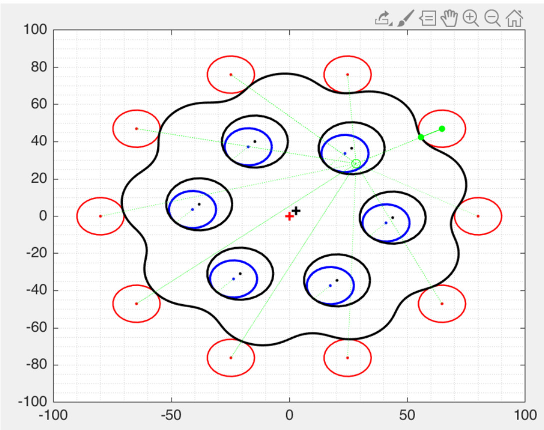

Figure 3.12: Profile after epicycloid generation and housing roller pin positions

As for the output roller which are fixed rigidly on the output shaft. The Figure 3.13 shows the points relevant to the vector required to define the force exchange between the cycloidal disk and the output pins.

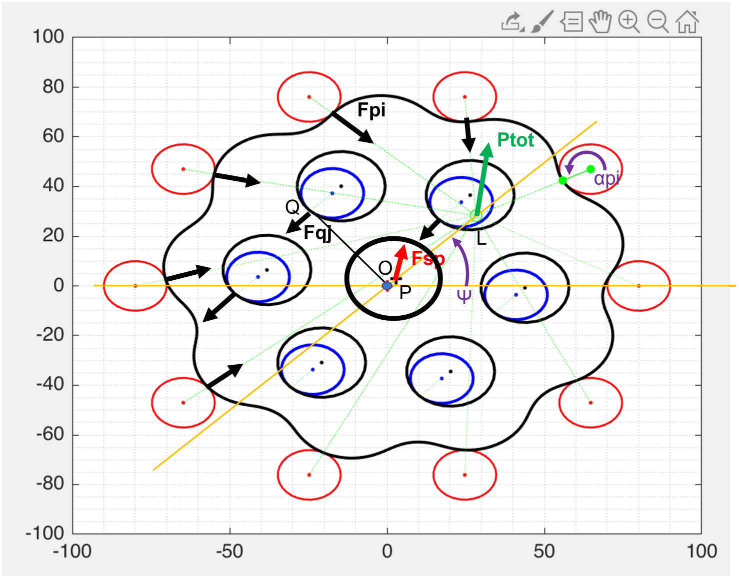

Figure 3.13: Geometric points relevant to the output shaft

The output roller center is defined the vector $\overrightarrow{OR}\,(n_{po},\psi)$:

$$\overrightarrow{OR}\,(n_{po},\psi) = R_{po}e^{i\left(\frac{\psi}{\tau}+\frac{2\pi}{N_{po}}(n_{po}-1)\right)} \tag{3.18}$$

While the center of the circle with radius R_{po}, where the output pins are located are given by the Equation 3.19.

$$\overrightarrow{OS}\,(n_{po},\psi) = \overrightarrow{OR} + \overrightarrow{OP} \tag{3.19}$$

The force acting on the point **Q** is defined by:

$$\overrightarrow{OQ}\,(n_{po},\psi) = \overrightarrow{OR} + \overrightarrow{RQ} \tag{3.20}$$

Where

$$\overrightarrow{RQ}\,(n_{po},\psi,a) = \frac{\left(\overrightarrow{OR} + \overrightarrow{OS}\right)}{|\overrightarrow{OR} + \overrightarrow{OS}|}R_{pin,o} \tag{3.21}$$

And the output action line is as follows:

$$F_{line,out}\,(n_{po},\psi,a) = \overrightarrow{OQ} + a\frac{\overrightarrow{RQ}}{|\overrightarrow{RQ}|} \tag{3.22}$$

3.4 Static Equilibrium

Static equilibrium can be written with the forces exchanged between the disk and rollers and the disk and the pins, but the forces have yet to be defined. Based on the working principal of the cycloidal drive there are several lobes in contact with the housing pins at any given time, futhermore since the system is statically indetermined, the equilibrium equations are insufficient to determine the exchanged forces, thus its assumed that the exchanged forces follows a sinusoidal distribution over span of ψ and $\psi + \pi$ (the contact forces are null outside the angular interval). However the forces exchanged between the disk and rollers tend to follow a sinusoidal distribution as highlighted below in Equation 3.26.

$$F_{pi} = |F_{pi}|e^{i\alpha_{pi}} \tag{3.23}$$

$$\alpha\left(n_{pr}, \psi\right) = \angle\left(F_{line} - \overrightarrow{OD}_{ring}\right) \tag{3.24}$$

$$|F_{pi}| = F_p|\sin\left(\alpha_{pi} - \psi\right)|c_{fi} \tag{3.25}$$

$$c_{fi} = \begin{cases} 1 & if\ \angle\overrightarrow{OD}_{ring} \in (\psi, \psi + \pi) \\ 0 & otherwise \end{cases} \tag{3.26}$$

However for the forces exchanged between the output pins and the disk are proportional to the arm of their torque moment as shown in Equation: 3.27. (As seen before in the above the section the subscript "j" in the following section denotes the j^{th} output pin)

$$F_{qj} = |F_{qj}|e^{i\alpha_{qj}} \tag{3.27}$$

$$\alpha\left(n_{po}, \psi\right) = \angle\left(F_{line,out} - \overrightarrow{OQ}\right) \tag{3.28}$$

$$|F_{qj}| = F_q b_j c_{fj} \tag{3.29}$$

$$b_j = Im\left(\overrightarrow{OQ}e^{-i\alpha_{qj}}\right) \tag{3.30}$$

$$c_{fj} = \begin{cases} 1 & if\ \angle\overrightarrow{OQ} \in (\psi, \psi + \pi) \\ 0 & otherwise \end{cases} \tag{3.31}$$

Considering all the forces experienced by the disk the **static translational equilibrium** can be represented in vectorial form by the Equation 3.32.

$$\sum_i F_{pi} + \sum_j F_{qj} + F_{s\mu} + F_{sp} + F_r = 0 \tag{3.32}$$

$$\Rightarrow F_p \sum_i c_{fi} |\sin(\alpha_{pi} - \psi)| e^{i\alpha_{pi}} + \mu_{sp} F_p \sum_i c_{fi} |\sin(\alpha_{pi} - \psi)| e^{i\left(\alpha_{pi} - \frac{\pi}{2}\right)} +$$
$$F_q \sum_j b_j c_{fj} e^{i\alpha_{qj}} + \mu_{sq} F_q \sum_j b_j c_{fj} e^{i\left(\alpha_{qj} - \frac{\pi}{2}\right)} + F_{sp} + \mu_{Fsp} F_{sp} e^{i\left(\psi_{Fsp} - \frac{\pi}{2}\right)} = 0 \tag{3.33}$$

Substituting:

$$\begin{aligned} A_{pi} &= c_{fi} |\sin(\alpha_{pi} - \psi)| \\ A_{qj} &= b_j c_{fj} e^{i\alpha_{qj}} \end{aligned} \tag{3.34}$$

Equation 3.32 now becomes:

$$\Rightarrow F_p \sum_i A_{pi} + \mu_{sp} F_p \sum_i A_{pi} e^{-i\frac{\pi}{2}} + F_q \sum_j A_{qj} + \mu_{sq} F_q \sum_j A_{qj} e^{-i\frac{\pi}{2}} + F_{sp}$$
$$+ \mu_{Fsp} F_{sp} e^{i\left(\psi_{Fsp} - \frac{\pi}{2}\right)} = 0 \tag{3.35}$$

Due to complex notation of the translation equation, two separate projections in the real and imaginary axis can be obtained. The vectorial equation above is broken into **Real** and **Imaginary** components similar to the **x axis** and **y axis**. Complex notation is used to write the equations because it avoids any complications arising from complex trigonometric relations.

However also the rotational equilibrium about the origin **O** is written in Equation 3.36.

$$\begin{aligned} &F_p \left(-Re\left(\sum_i A_{pi}\right) Im\left(\overrightarrow{OL}\right) - Im\left(\sum_i A_{pi}\right) Re\left(\overrightarrow{OL}\right)\right) + \\ &\mu_{sp} F_p \left(\left(\sum_i Re\left(A_{pi} e^{-i\frac{\pi}{2}}\right) Im\left(\overrightarrow{OD}\right)\right) + \left(\sum_i Im\left(A_{pi} e^{-i\frac{\pi}{2}}\right) Re\left(\overrightarrow{OD}\right)\right)\right) + \\ &\mu_{sq} F_q \left(\left(\sum_i Re\left(A_{qj} e^{-i\frac{\pi}{2}}\right) Im\left(\overrightarrow{OQ}\right)\right) + \left(\sum_i Im\left(A_{qj} e^{-i\frac{\pi}{2}}\right) Re\left(\overrightarrow{OQ}\right)\right)\right) + \\ &F_q \left(\sum_j \left(-Re\left(A_{qj} Im\left(\overrightarrow{OQ}\right)\right) + \sum_j \left(Im\left(A_{qj}\right) Re\left(\overrightarrow{OQ}\right)\right)\right)\right) + \\ &-Re\left(F_{sp}\right) Im\left(\overrightarrow{OP}\right) + Im\left(F_{sp}\right) Re\left(\overrightarrow{OP}\right) + \\ &\mu_{Fsp} Im\left(F_{sp}\right) Re\left(D_{shaft}\right) + \mu_{Fsp} Re\left(F_{sp}\right) Im\left(D_{shaft}\right) = 0 \end{aligned} \tag{3.36}$$

After having solved the static equilibrium problem the forces acting on the disk can be calculated and displayed along with the accompanying friction forces as shown in Figure 3.14.

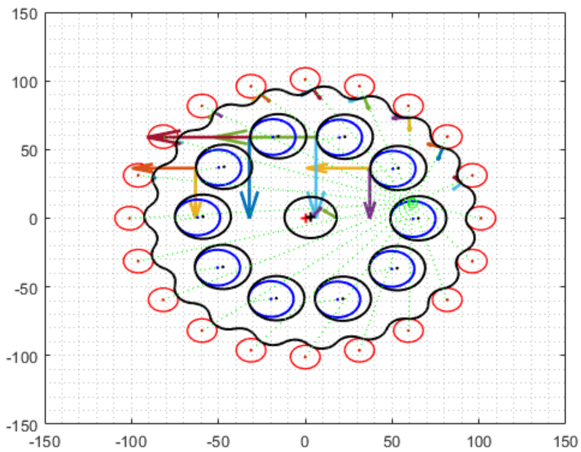

Figure 3.14: All the forces acting on the cycloidal disk at a given instance

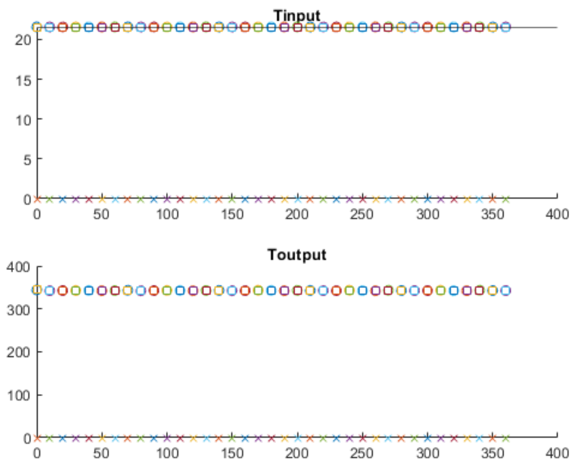

Figure 3.15: Input and Output torque of the drive as a function of the input shaft angle

The model presents a constant torque throughout the entire rotation of the input shaft, this is confirmed by the torque calculated by the model in Figure 3.15. The force distribution related to the contact forces acting on the disk are shown in Figure 3.16.

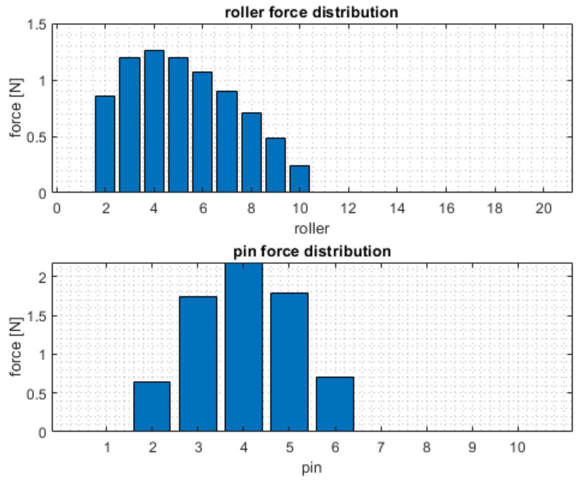

Figure 3.16: Force distribution acting on the disk

3.5 Friction Model

The concept of sliding friction was introduced in order to have a more realistic outcome from the simulations. This involved assigning a friction coefficient for each type of contact force, however to simplify the simulation the same magnitude of the friction coefficient is applied for both types of contact forces;roller-disk contacts and pin-disk contacts. The introduction of friction results in a force that is perpendicular to any contact force with a vector that opposes the motion of the disk and a resultant magnitude proportional to the contact force by means of the friction coefficient.

In order to verify if the mathematical model with friction tends to follow a realistic case, the parameters and experimental data of literature sources are used to compare the calculated efficiency and output torque with the efficiency and output torque provided in the literature.

3.5.1 Literature Source: Politecnico di Milano

Notice the configuration of the drive which is similar in terms of the configuration of the Cyclo6000 Reducer initially selected for this application. In this model sliding friction is considered between all three possible sources between; the disk and rollers, the disk and pins and finally between the input shaft and disk.

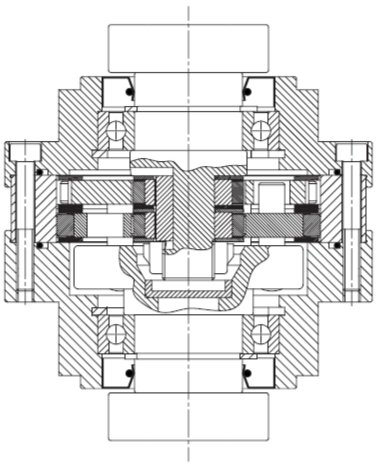

Figure 3.17: Cross section of the drive[15]

The friction coefficient for the input shaft is a fixed predetermined value while the friction coefficient for the rollers and pins are determined by a quadratic relationship involving the input torque as shown in Equation 3.37.

$$f_p = f_q = a{M_{in}}^2 + bM_{in} + c \tag{3.37}$$

Speed (rpm)	M_{in} (N m)	f (/)	η_{theo} (/)	η_{exp} (/)	Δ (%)
500	2.9	0.045	0.76	0.75	−1.3
500	3.9	0.033	0.81	0.78	−3.8
500	4.6	0.029	0.84	0.83	−1.2
500	5.4	0.026	0.85	0.88	3.4
1000	2.9	0.045	0.76	0.75[a]	−1.3
1000	3.7	0.035	0.80	0.81[a]	1.2
1000	4.6	0.029	0.84	0.83[a]	−1.2
1000	5.6	0.026	0.85	0.85[a]	0.0
1500	3.1	0.042	0.77	0.72	−6.9
1500	3.9	0.033	0.81	0.79	−2.5
1500	4.9	0.027	0.84	0.80	−5.0
1500	5.6	0.026	0.85	0.85	0.0
2000	3.2	0.041	0.77	0.71	−8.5
2000	4.0	0.033	0.82	0.81	−1.2
2000	4.7	0.028	0.84	0.85	1.2
2000	5.4	0.026	0.85	0.89	4.5

[a]Results used for the calibration of the model.

Figure 3.18: Experimental data[15]

M_{in} represents the input torque in this case, while the constants a, b, and c are determined by means of the experimental data provided in Figure 3.18 rated at a 1000 rpm. In Table 3.1 the experimental data is utilised to extrapolate the quadratic coefficients.

Speed [rpm]	M_{in} [Nmm]	f
1000	2900	0.045
1000	3700	0.035
1000	4600	0.029
1000	5600	0.026
a $[Nmm^{-2}]$	b $[Nmm^{-1}]$	c [-]
2.58E-09	-2.89E-05	0.1069

Table 3.1: Experimental data used to calculate friction coefficients[15]

It must be mentioned that not all geometric parameters were specified in the literature so some parameters were reasonable estimated such as the diameter of the input shaft. Although the friction coefficient between the input shaft and disk is quite low and thus contributes to a low portion of the losses.

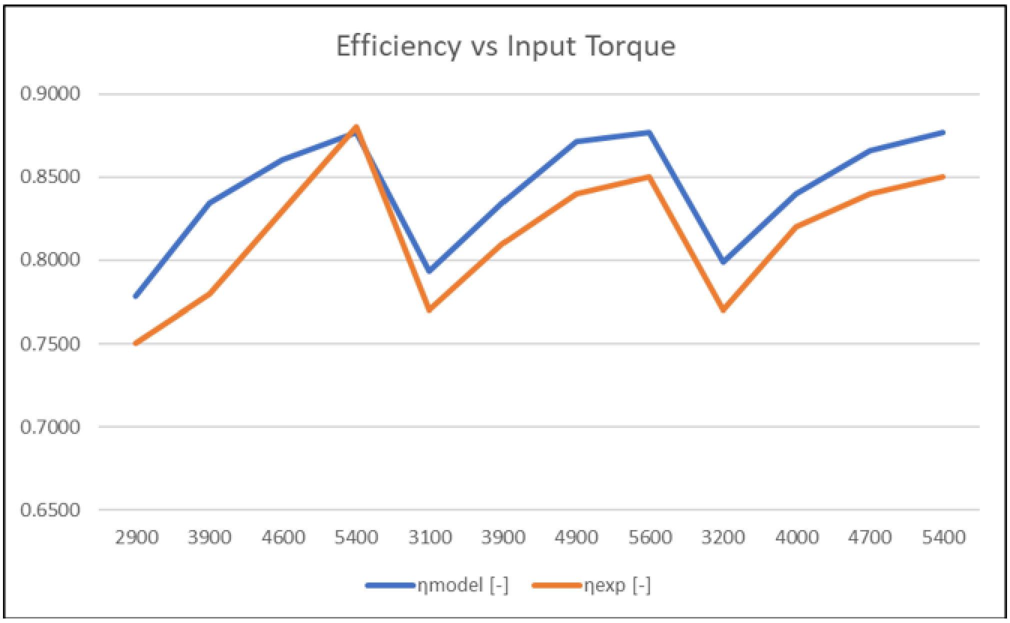

Figure 3.19: Efficiency of the model versus the experimental efficiency data[15]

In Figure 3.19 the efficiency of the model is similar for the majority of input torque operating range. The shift in efficiency values between the two models can be attributed to difference in the geometry parameters, since the trend is the fairly similar, however its shift is roughly constant.

3.5.2 Literature Source: Lodz University

In this model like in the above mentioned model, friction is present in between; the disk and roller, the disk and pins and the disk and the input shaft. The friction model utilized in the model is also sliding friction without rolling friction. In addition to reporting the values of the efficiency from the bench test, the relationship between the input and output torque is also reported. In the Figure 3.20 is shown and it can be seen that for both the housing rollers and output pins sliding elements have reduced the effect of friction losses.

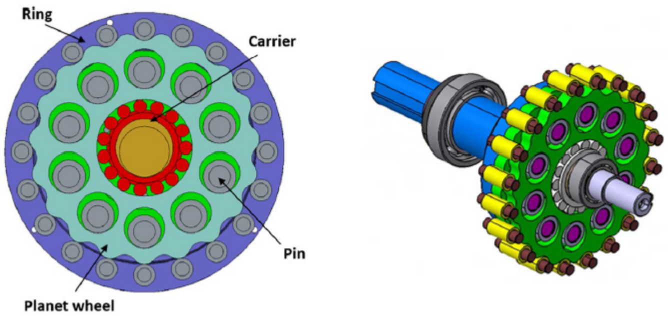

Figure 3.20: Configuration of the Lodz gearbox[16]

A particular feature about this model is that at the beginning it makes use of a linear force for the transmission between the input shaft and the disk, this results is an efficiency that is independent of the imposed output torque. So the expected trend for the computed efficiency is seen in the Figure 3.20 by the fact that the efficiency is a straight line covering the entire operating range. Moreover the actual trend for the efficiency tends to be heavily dependent on the imposed output torque and tends to increase as the torque increases before reaching a saturation level. Later on in the latter stages of this work a non-linear force is suggested in place of the linear force because it characterises the deformation of the components within the drive and explains the reason behind the link between the of the efficiency of the model and the imposed output force.

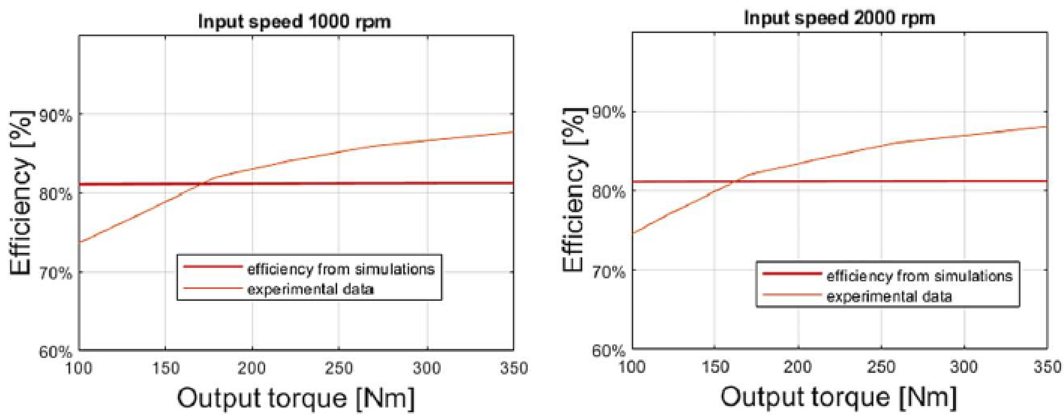

Figure 3.21: Efficiency of the Lodz model[16]

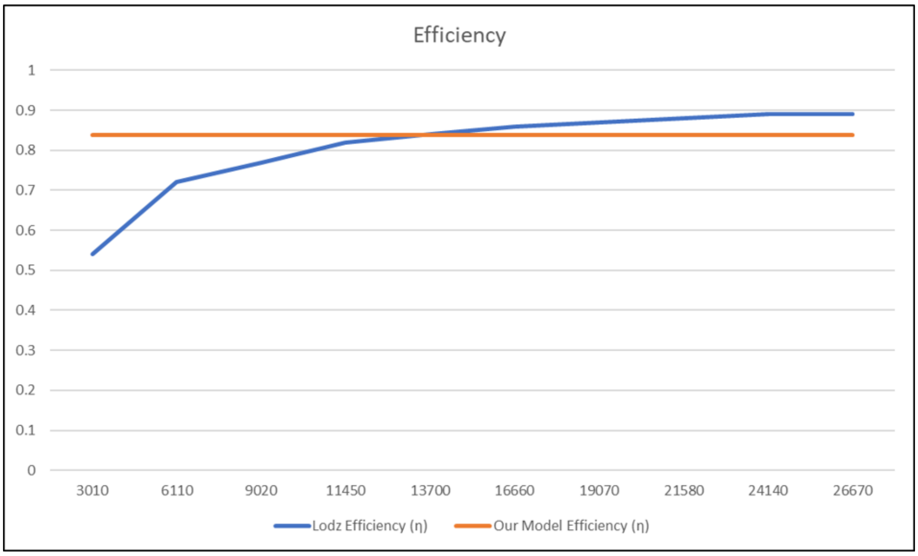

Figure 3.22: Efficiency for the linear Matlab model

In the Figure 3.23 the input versus output torque for both the Matlab model and the Lodz models shows a close overlap which further proves that the model is sufficiently accurate in order to the simulate the operation of the drive.

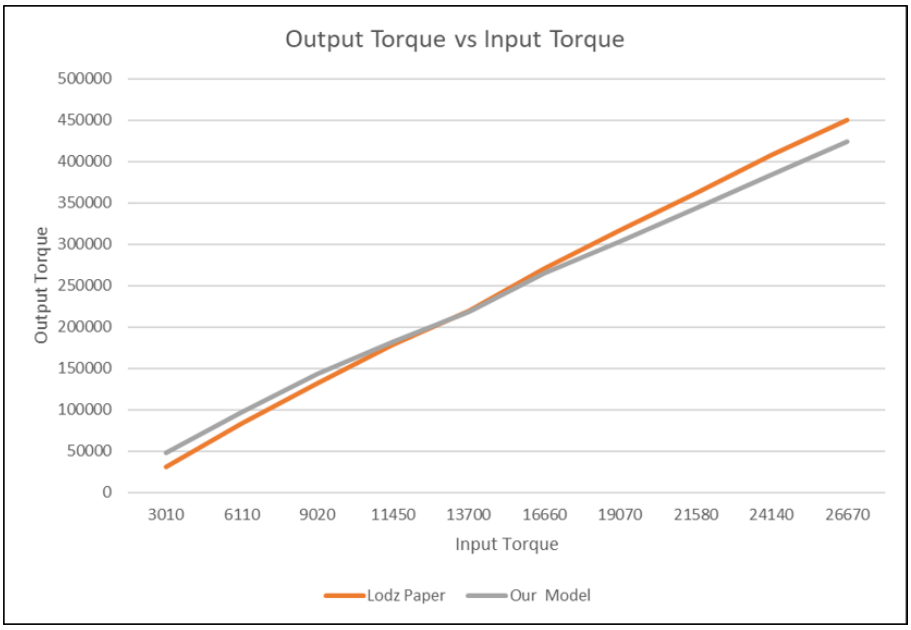

Figure 3.23: Input torque versus output torque

3.6 Internal Reactions

Another consideration must be made for the internal reactions experienced by the drive and thus also the bearings within the drive. The first step is to determine the force exchanged within the drive, then calculating the internal reactions. The forces exchanged between the rollers and pins and the disk are obtained by solving the static equilibrium equation.

To identify the internal reaction it is necessary to view the gearbox from two perpendicular views with respect to the central axis of the gearbox, preferable the **XZ** and **YZ** reference frames like in Figure 3.24. The figure below is just an example of the reference frame used for the YZ view.

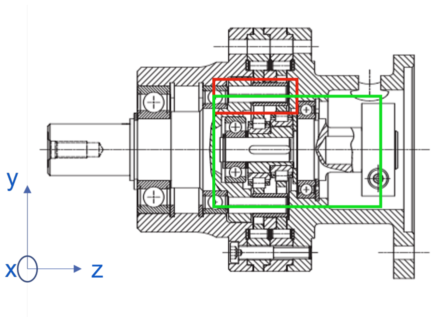

Figure 3.24: YZ reference frame used for the internal reaction calculation[8]

Figure 3.25a and 3.25b shows a close up view of the of the YZ reference frame applied to the output pin and input shaft respectively. The reason why the focus of the internal reaction is shift towards the output pins and the input shaft is because its the most critically stressed section of the gearbox.

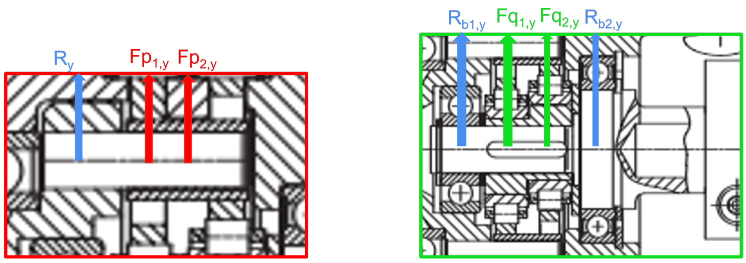

(a) YZ Reference frame for the pin

(b) YZ Reference frame for the input shaft

Figure 3.25: Reference frame used for the internal reaction calculation

3.6.1 Input Shaft Internal Reactions

Using Figure 3.26 and 3.27 as a reference for the reaction forces, they can be calculated using the Equation 3.39 and 3.41 which can be obtained by first solving the reaction forces in Equation 3.38 and 3.40.

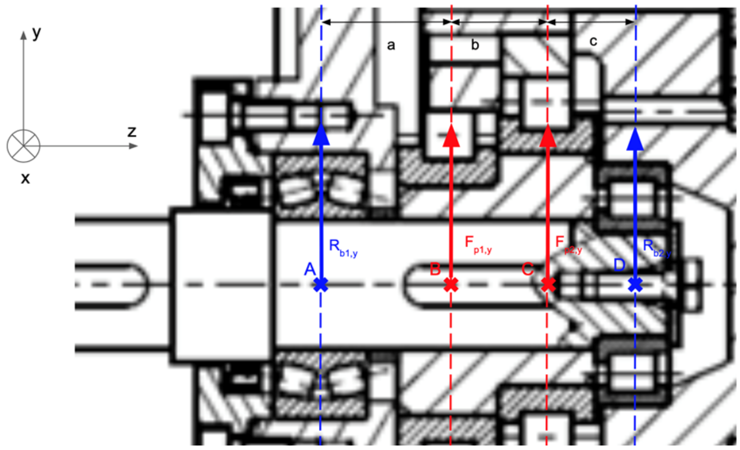

Figure 3.26: Close up of YZ reference frame for the input shaft

$$\begin{aligned} R_{b1,y} + F_{p1,y} + F_{p2,y} + R_{b2,y} = 0 \\ aF_{p1,y} + (a+b)F_{p2,y} + LR_{b2,y} = 0 \end{aligned} \tag{3.38}$$

$$M_{fx} = \begin{cases} -zR_{b1,y} & if\ z\ \in [0,a] \\ -[(a+b-z)F_{p2,y} + (L-z)R_{b2.y}] & if\ z \in [a,a+b] \\ -(L-z)R_{b2,y} & if\ z\ \in [a+b,L] \end{cases} \tag{3.39}$$

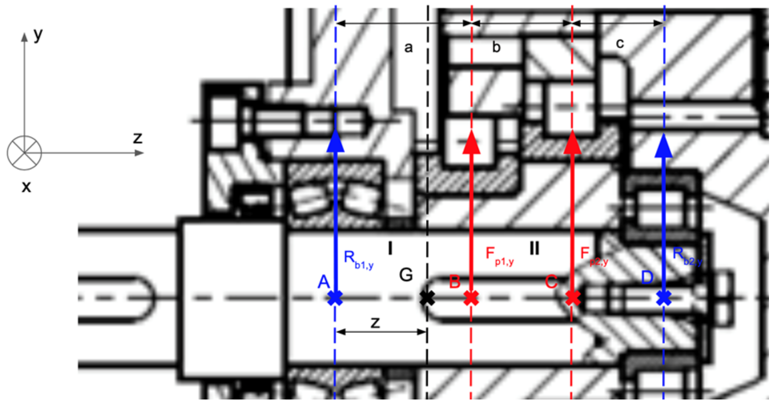

Figure 3.27: Close up of XZ reference frame for the input shaft

$$
\begin{aligned}
R_{b1,x} + F_{p1,x} + F_{p2,x} + R_{b2,x} &= 0 \\
aF_{p1,x} + (a+b)F_{p2,x} + LR_{b2,x} &= 0
\end{aligned}
\tag{3.40}
$$

$$
M_{fy} = \begin{cases} zR_{b1,x} & if\ z\ \in [0,a] \\ -[(a+b-z)F_{p2,x} + (L-z)R_{b2.x}] & if\ z \in [a, a+b] \\ (L-z)R_{b2,x} & if\ z\ \in [a+b, L] \end{cases}
\tag{3.41}
$$

3.6.2 Output Pin Internal Reactions

The same procedure can be used as the one in the section regarding the input shaft internal reaction. The output pins are much more critical as they bare a higher load on a smaller area.

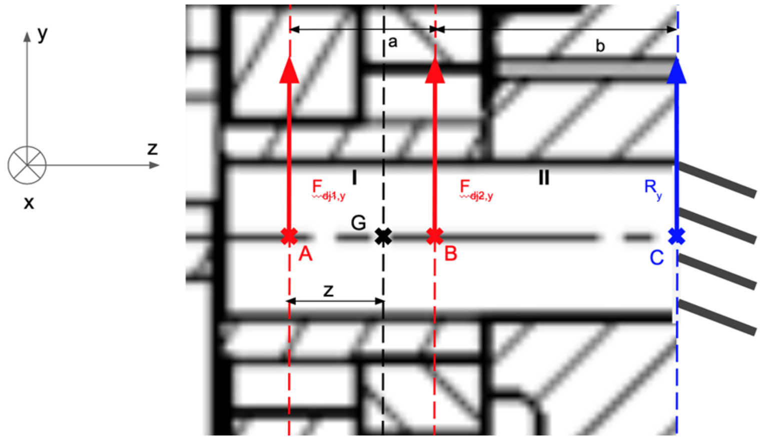

Figure 3.28: Close up of YZ reference frame for the output pin

$$
F_{dj1,y} + F_{dj2,y} + R_y = 0 \tag{3.42}
$$

$$
M_{fx} = \begin{cases} -zF_{dj1,y} & if\ z\ \in [0,a] \\ -(L-z)R_y & if\ z \in [a, L] \end{cases}
\tag{3.43}
$$

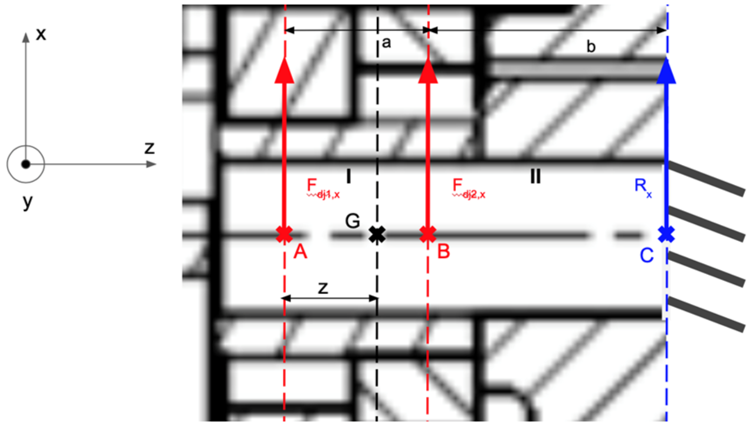

Figure 3.29: Close up of XZ reference frame for the input shaft

$$F_{dj1,x} + F_{dj2,x} + R_x = 0 \tag{3.44}$$

$$M_{fy} = \begin{cases} zF_{dj1,x} & if\ z\ \in [0, a] \\ (L - z)R_x & if\ z \in [a, L] \end{cases} \tag{3.45}$$

The actual value of the forces acting on the input shaft and output pins vary as the disk rotates, so in order to calculate the internal reactions for a given rotation angle of the disk. This angle must also be the same for the calculation of the other internal reaction in the other reference frame.

The bending moment from each plane is coupled together and utilising the Von Mises stress criterion (σ_{Mises}) along with the yield strength of the material to establish whether is satisfies the safe factor.

$$\begin{aligned} M_f &= \sqrt{M_{fx}^2 + M_{fy}^2} \\ \overline{\sigma}_{Mises} &= \sqrt{\sigma^2 + 3\tau^2} \\ I_0 &= \frac{\pi R^4}{2} \\ \sigma_{Mises} &= \frac{M_f}{I_0} R \\ \tau &= \frac{M_t}{I_0} \\ S_F &= \frac{\sigma_y}{\sigma_{Mises}} \end{aligned} \tag{3.46}$$

The resultant bending and individual bending in each plane are shown below in for the input shaft and output pin, in Figure 3.30b and 3.31b respectively.

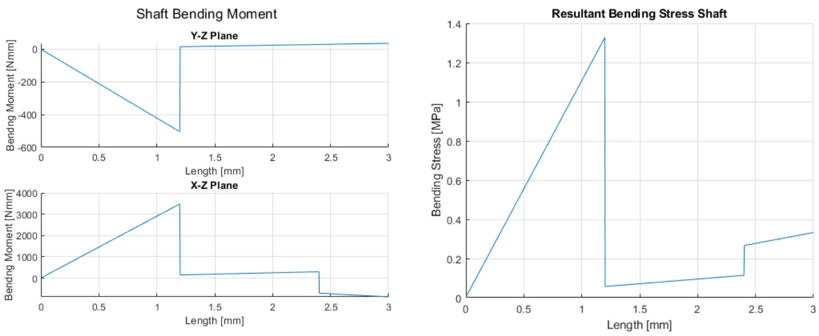

(a) bending for the input shaft in each plane

(b) Resultant bending for the input shaft

Figure 3.30: Input shaft bending stress

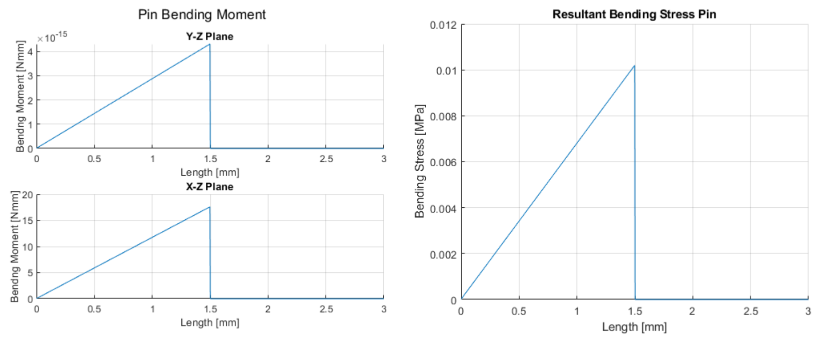

(a) bending for the Output pin in each plane

(b) Resultant bending for the Output pin

Figure 3.31: Output pin bending stress

3.7 Hertzian Contact

Due to the nature of the contact forces an analysis regarding the hertzian pressure experienced by the pins, rollers and more importantly the cycloidal disk must be undertaken. The hertzian stress poses the greatest risk from the point of view of yielding which will not cause immediate failure, but can lead to progressive damage.

3.7.1 Hertz Theory

The basic concept behind hertzian contact is a method of establishing the stress experienced by two bodies in contact. In an ideal world the contact between rigid bodies is a type of point contact without any deformation. Unfortunately in reality the contact isn't a single point, but rather a surface coupled with the deformation of both elastic bodies.

In the case of the cycloidal drive there are two major areas of interest:

1. Disk - Housing Roller contact
2. Disk - Output Pin contact

In general, based on the type of convex or concave nature of the contact the curvatures must be obtained accordingly. Naturally due to the type of contact the curvature in the reference frame along the length of the disk is null because the radius is infinite.

In the following expressions develop the formula needed for the general approach for the hertz contact.

The curvature of each surface becomes:

$$\rho_{i,j} = \pm \frac{1}{R_{i,j}} \tag{3.47}$$

The subscript i and j referring to the each body involved in the contact, since the contact requires looking at the bodies in contact with two independent and orthogonal reference frames. The sign involved in the curvature is dependent on whether they represent a convex to convex contact or a concave to convex contact like in Figure 3.32.

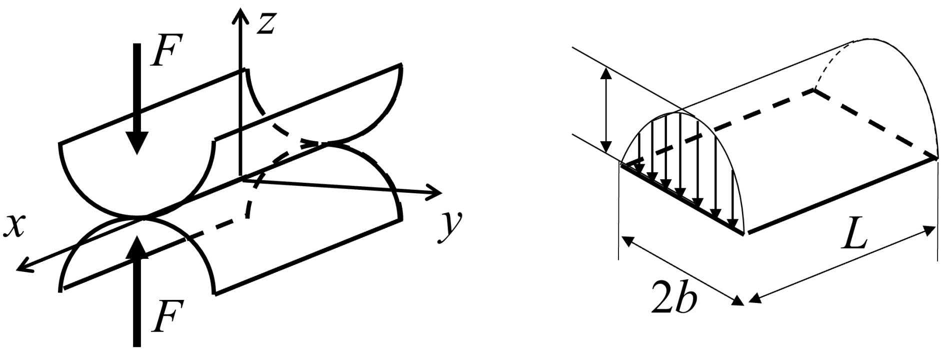

Figure 3.32: Example of concave to concave contact with a close view of the contact area[17]

Subsequently the semi-width of the area of contact of the disk is achieved through:

$$b = \sqrt{\frac{P(\theta_1 + \theta_2)}{\pi l \Sigma \rho_{i,j}}} \tag{3.48}$$

Where

$$\theta = 4\frac{1 - \nu^2}{E} \tag{3.49}$$

The external concave cylinder provides the largest contribution assures that the argument within the square root is positive. With the value of the semi-width this allows the calculation of the mean stress experienced by the contact area.

$$\sigma_m = \frac{P}{A} = \frac{P}{2bl} \tag{3.50}$$

Through empirical formulae the maximum stress is distributed along the line of symmetry at the center of the area of contact.

$$\sigma_0 = \frac{4\sigma_m}{\pi} \tag{3.51}$$

However with semi-empirical formula for certain materials like steel for example leads to simplified grey box model: (ρ^* is the summation of all the curvature)

$$b = 1.522\sqrt{\frac{P}{l\rho^* E^*}} \tag{3.52}$$

The overall Young's modulus becomes:

$$E^* = \frac{2}{\frac{1}{E_1} + \frac{1}{E_2}} \tag{3.53}$$

Utilizing this grey model, both the mean stress and the maximum stress can be obtained through Equations 3.54 and 3.55. An important clarification must be made that the link between the maximum stress and the equivalent stress is based on the Mohr's circle and is 60% of the maximum stress. The most stressed section isn't located on the surface but slightly below the surface, although its location isn't required in this analysis.

$$\sigma_{max} = 0.418\sqrt{\frac{P\rho^* E^*}{l}} \tag{3.54}$$

$$\sigma_{eq} = 0.2508\sqrt{\frac{P\rho^* E^*}{l}} \tag{3.55}$$

3.7.2 Hertz Contact Output Pins

The contact between the disk and the output pin case produces the easier of the two cases to deal with initially. Figure 3.33 shows the highlighted area of interest and also shows the general case of hertzian contact for cylinder to cylinder contact.

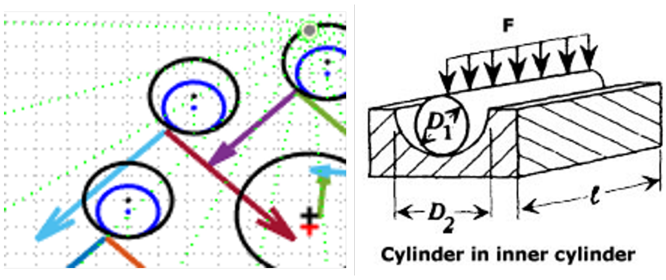

Figure 3.33: Contact between the output pin and disk[18]

In the case of the output pin scenario the surfaces form a convex to convex case. The curvature of each surface involved and thus the radius of the surface are constant throughout the rotation of the disk. For each rotation of the disk the hertzian stress acting on the pin has to to be constantly calculated because naturally the force experienced by each pin varies as the disk rotates.

The curvature for each of the surfaces becomes:

- Output Pins

$$\begin{aligned} \rho_{11} &= +\frac{1}{R_{pin}} \\ \rho_{12} &= 0 \end{aligned} \tag{3.56}$$

- Disk

$$\begin{aligned} \rho_{21} &= 0 \\ \rho_{22} &= -\frac{1}{R_h} \end{aligned} \tag{3.57}$$

The equivalent stress is not only a function of the angle of the disk but also the number of the pin to which it refers to like the formula shown in Equation 3.58.

$$\sigma_{eq,j}(\psi, n_{po}) = 0.2508\sqrt{\frac{F_{qj}(\psi, n_{po})E\rho}{hR_{pin}(R_{pin}+\rho)}} \tag{3.58}$$

3.7.3 Hertz Contact Housing Rollers

The case regarding the contact of the disk and the roller involves another level of complexity due to the irregular profile of the disk.

The curvature for each of the surfaces becomes:

- Housing Roller

$$\begin{aligned} \rho_{11} &= +\frac{1}{R_r} \\ \rho_{12} &= 0 \end{aligned} \tag{3.59}$$

- Disk

$$\begin{aligned} \rho_{21} &= 0 \\ \rho_{22} &= +\frac{1}{R_T(\psi)} \end{aligned} \tag{3.60}$$

The equivalent stress like before is a function of the rotation angle of the disk and the particular roller which it is referring to.

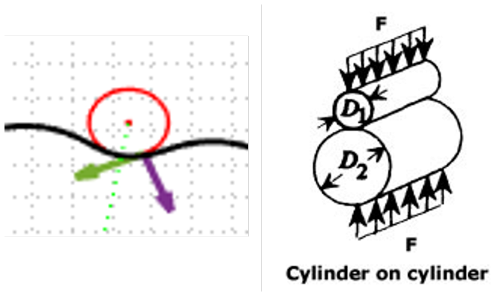

Figure 3.34: Contact between the housing roller and disk[18]

$$\sigma_{eq,i}(\psi, n_{pr}) = 0.2508\sqrt{\frac{F_{pi}(\psi, n_{pr})(\frac{1}{R_r} + \frac{1}{R_T})E}{h}} \tag{3.61}$$

The stress experienced by each pin and roller is reported in Figure 3.35, notice that the output pins tend to carry a higher load than the rollers. It seems intuitive since the whole objective is for the cycloidal drive to amplify the output torque and the output pins are the elements used to transmit that torque.

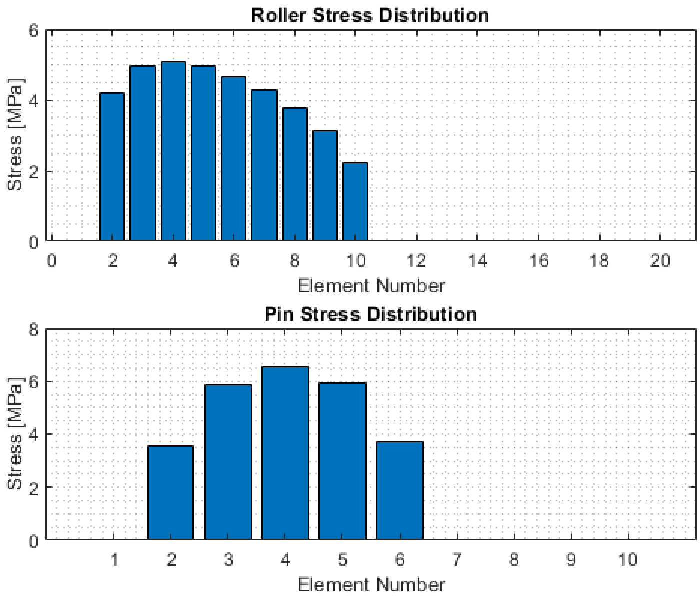

Figure 3.35: Stress experienced by pins and rollers

3.7.4 Minimum Thickness

Determining the minimum thickness of the cycloidal disk can be done by identifying the thickness required if the stress experienced by the output pin is equivalent to the admissible stress of the material considering the safety factor. If the admissible thickness is **above** the predefined default thickness then it becomes the recommended thickness. The reason why the output pin is used for this purpose is because it experiences a higher force then the housing rollers and the force is proportional to the stress.

$$\begin{aligned} \sigma_{adm} &= \frac{\sigma_y}{S_F} \\ h_{adm}(F_{qj}, \psi) &= \left[\frac{F_{qj} E \rho}{R_{pin}(R_{pin} + \rho)}\right] \left(\frac{0.02508}{\sigma_{adm}}\right)^2 \end{aligned} \tag{3.62}$$

Naturally the thickness must be calculated throughout the rotation of the input shaft and also for each pin hence the admissible thickness (h_{adm}) in Equation 3.62. The equation comes from reverse engineering the grey model formula for steel in 3.61.

Fortunately given the current working conditions the default thickness set as 5 mm is never compromised.

3.8 Profile Singularity

Another consideration is the feasibility of the design of the cycloidal disk. This section focuses on the curvature of the disk because the machining process which produce the disk has to be capable of creating a smooth profile which translates to a smooth performance of the machine.

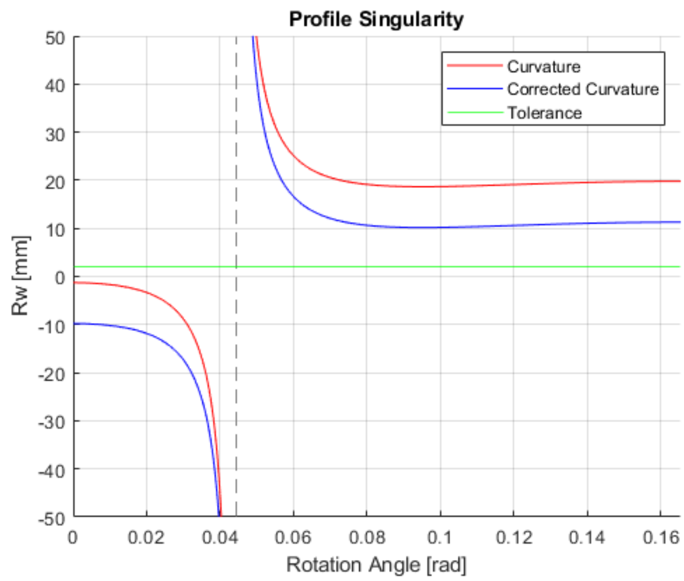

Figure 3.36: Profile singularity curve

The curvature profile (R_W) in **red** generated in Figure 3.36 is achieved by calculating the vector $\overrightarrow{PA}$ in terms of a parametric equation in based on Cartesian coordinates rather than in complex notation. The parametric equation are shown in Equation 3.63.

The profile must be corrected keeping in mind that the profile generated by the vector $\overrightarrow{PA}$ is the center of the housing roller and therefore must shift by the radius of the roller, thus providing the **blue** correct curvature profile (R_T).

The machine tolerance is a constant specified beforehand and if the corrected curvature profile were to fall below this threshold it would resultant in an infeasible profile like in Figure 3.37b. In a practical sense an infeasible profile is when the curvature must take sudden change in direction when constructing the disk which will result in an irregular surface and it undesirable.

Only a certain portion has been reported in Figure 3.36 since it a symmetric in nature across each lobe, thus only half the rotation over the first lobe has been portrayed.

(a) Example of feasible profile (b) Example of infeasible profile

Figure 3.37: Example of disk profiles

The curvature of any surface is obtained through the inverse of the radius of the surface. The radius of the surface is broken down into its constitute x and y components in Equation.

$$\begin{Bmatrix} x_T = (R_p + R_g)cos(\theta) - \rho cos[\theta(1 + z_1)] \\ y_T = (R_p + R_g)sin(\theta) - \rho sin[\theta(1 + z_1)] \end{Bmatrix} \tag{3.63}$$

The radius for the parametric equation is:

$$K = \frac{|\frac{\partial x \partial^2 y}{\partial \theta \partial \theta^2} - \frac{\partial^2 x \partial y}{\partial \theta \partial \theta^2}|}{\left[(\frac{\partial x}{\partial \theta})^2 + (\frac{\partial y}{\partial \theta})^2\right]^{\frac{3}{2}}} \tag{3.64}$$

Since the definition of the curvature is the inverse of the parametric radius:

$$R_K = \frac{\left[(\frac{\partial x}{\partial \theta})^2 + (\frac{\partial y}{\partial \theta})^2\right]^{\frac{3}{2}}}{|\frac{\partial x \partial^2 y}{\partial \theta \partial \theta^2} - \frac{\partial^2 x \partial y}{\partial \theta \partial \theta^2}|} \tag{3.65}$$

The theoretical and the corrected curvatures of the profile is as follows in Equation 3.66 and 3.67 respectively.

$$R_T = \frac{\left[\frac{m}{2}(z_1 + 1)^2(1 - 2(1 - x)cos(z_1\theta) + (1 - x)^2)\right]^{\frac{3}{2}}}{1 - (1 - x)(2 + z_1)cos(z_1\theta) + (1 - x)^2(1 + z_1)} \tag{3.66}$$

$$R_w = R_T - R_r \tag{3.67}$$

Certain key geometric parameters are introduced in order to make the relationship between some of the major dimensions with a principle parameter such as the module in Equations 3.68, 3.69, and 3.70. Followed by the substitution of the below parameters into Equation 3.65 with its respective derivatives.

$$m = 2R_g \tag{3.68}$$

$$R_{ring} = R_p + R_g \tag{3.69}$$

$$R_{ring} = \frac{m}{2} + \frac{z_1 m}{2} = \frac{(z_1 + 1)m}{2} \tag{3.70}$$

3.9 Equivalent Inertia

The layout of the components needs to be considered to evaluate the equivalent inertia of the drive because not only does it give a measure of the distribution of the mass. Figure 3.38 shows the general components which influence the equivalent inertia and are listed below:

- Cycloidal disk
- Input shaft
- Output pins
- Holes for the Output pins
- Housing rollers

Many of the above listed elements do not lay on the central axis of rotation therefore **Huygens Steiner's** principle will be taken advantage off. This principle allows the consideration of the inertia of multiple objects that does not lay on the principle axis of rotation to establish an equivalent inertia that seems to rotate about the original axis of rotation.

$$I = I_c + Mh^2 \tag{3.71}$$

In Huygens Steiner's principle reported in Equation 3.71 I_c denotes the original inertia in terms on the central axis of rotation of the body while the M and h^2 represents the mass and the distance between the two axes of rotation for I and I_c.

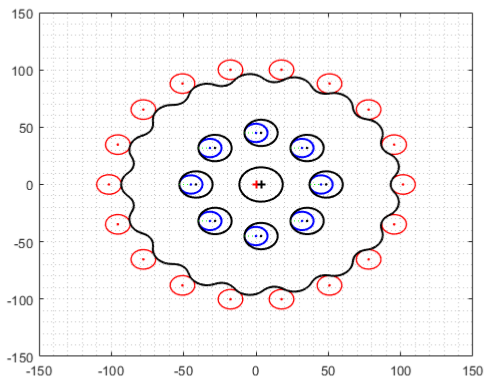

Figure 3.38: Layout of the elements within the drive

For each of the elements the inertia formulation will be reported in the following equations.

$$I_{eq} = I_{disk} + I_{output-pins} - I_{output-holes} + I_{housing-rollers} \tag{3.72}$$

$$I_{housing-rollers} = \Sigma_i^{Npr} \frac{1}{2} m_{roller} R_{r,i}^2 + \frac{1}{2} m_{roller} l_{roller,i}^2 \tag{3.73}$$

$$I_{housing-pins} = \Sigma_j^{Npo} \frac{1}{2} m_{pin} R_{pin,j}^2 + \frac{1}{2} m_{pin} l_{pin,i}^2 \tag{3.74}$$

$$I_{housing-holes} = \Sigma_j^{Npo} \frac{1}{2} m_{holes} R_{h,j}^2 + \frac{1}{2} m_{holes} l_{holes,i}^2 \tag{3.75}$$

$$I_{disk} = I_o + \frac{1}{2} m_{disk} OP^2 \tag{3.76}$$

$$I_o = \frac{1}{2} m_{disk} r_{disk,eq}^2 \tag{3.77}$$

Given the irregular profile of the disk it doesn't have a predefined constant radius therefore an equivalent radius has to be assessed which is roughly estimated as radius along which all the housing rollers are located (the vector $\overrightarrow{PA}$ described in the geometry scetion).

Chapter 4

Optimisation

All the previous sections were needed to evaluate the overall performance of the gearbox and establish objective functions for the optimization process. Apart from the objective functions also the geometric constraints need to be respected throughout the process.

The main **two** objective functions are:

1. Efficiency
2. Equivalent Inertia

As for the free variables for the optimization problem there are **five** geometric parameters which govern the overall performance of the gearbox:

1. Housing roller radius (R_r)
2. Output roller radius (R_{pin})
3. Output pin circle radius (R_{po})
4. Housing pin circle radius (R_p)
5. Modification factor (x_{mod})

Before moving on towards the type of solver **two** other parameters needs to be clarified; the bounds of the free variables, and operating characteristics. The bounds are determined by the logical values such as for the lower bounds a non negative or null value and the on the other hand the upper bound is based on the available space. The **three** operating characteristics are:

- Transmission ratio = 77

- Input torque = 455 Nm
- Housing radius = 85 mm

Based on the **complexity of the problem** and the **number of free variables** together with the **nature of the constraints** the proposed type of optimisation process is the **Genetic Algorithm**.

4.1 Sensitivity Analysis

As a prelude to the optimisation a sensitivity analysis is conducted to have an understanding of what to expect from the optimisation in terms of results. The basic working principle of the analysis is to have a set of control parameters and then varying one of the geometric parameter while keeping the other control parameters fixed to establish its effect on the overall performance.

Control simulation parameters:

- Number of housing rollers (N_{pr}): 19
- Number of output pins (N_{po}): 10
- Housing roller radius (R_r): 8.5 mm
- Output roller radius (R_{pin}): 62 mm
- Output pin circle radius (R_{po}): 13 mm
- Housing pin circle radius (R_p): 96 mm
- Modification factor (x_{mod}): 0.38 mm

There are three different outputs that are viewed as a way to understand its effects; efficiency, output torque and equivalent inertia.

The efficiency of the gearbox is a direct consequence of the output torque since its other parameters are imposed as shown in Equation 4.1. Therefore it is expected to see the same trend between the efficiency and the output torque.

$$\eta = \frac{T_{output}\omega_{in}}{T_{input}\omega_{out}} = \frac{T_{output}}{T_{input}\tau} \tag{4.1}$$

When it comes to the equivalent inertia, its value is solely based on the values assigned to the geometric parameters and the formulae described in the aforementioned section regarding the equivalent inertia.

4.1.1 Housing roller radius

Firstly there is a positive correlation between the efficiency and equivalent inertia and the radius variation, however the variation of the roller radius is not a good choice due to its slight variation of the efficiency and larger increase in equivalent inertia.

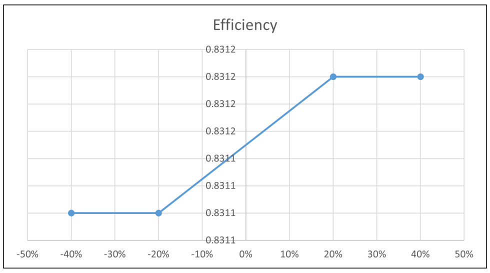

Figure 4.1: Efficiency Variation

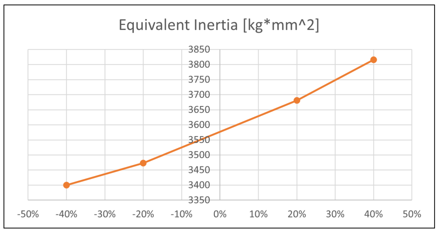

Figure 4.2: Equivalent Inertia Variation

4.1.2 Output roller radius

As seen with the housing roller radius, it also has a positive correlation for both trends. The variation of the output pin radius offers only a slight in efficiency and a higher increase in the equivalent inertia.

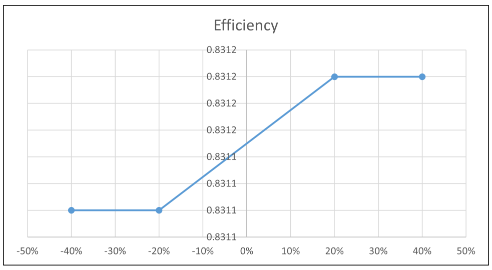

Figure 4.3: Efficiency Variation

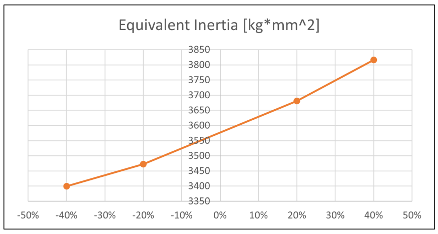

Figure 4.4: Equivalent Inertia Variation

4.1.3 Output pin circle radius

Again there is a positive correlation for both trends, however in this case it is actually worth varying the output pin circle radius for increased performance.

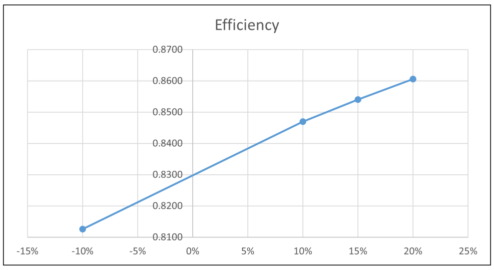

Figure 4.5: Efficiency Variation

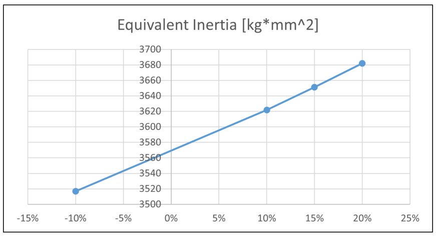

Figure 4.6: Equivalent Inertia Variation

4.1.4 Housing pin circle radius

The housing pin circle radius parameter has a positive correlation for the equivalent criteria, but a negative correlation for the efficiency which does not make it a good choice to modify for performance gains.

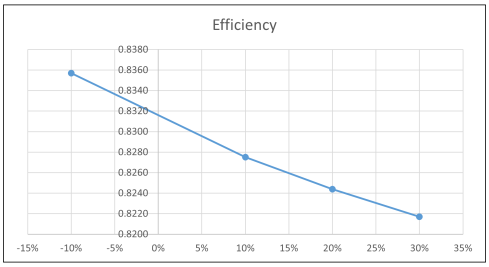

Figure 4.7: Efficiency Variation

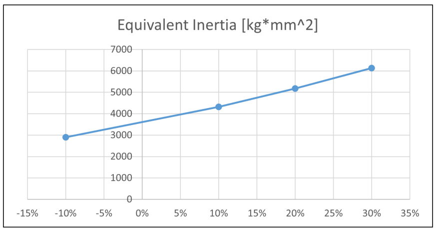

Figure 4.8: Equivalent Inertia Variation

4.1.5 Modification factor

Like the parameter above there is a positive correlation for the equivalent inertia and a negative correlation for the efficiency. These correlations highlight that this is not a suitable parameter for modification for performance gains.

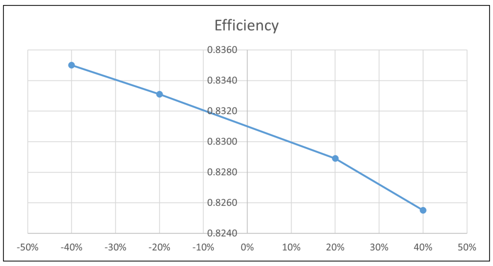

Figure 4.9: Efficiency Variation

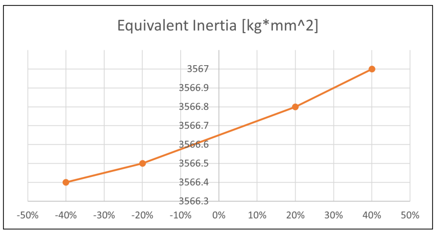

Figure 4.10: Equivalent Inertia Variation

4.1.6 Number of output pins

The effect of the number of output pins have a minimal effect on the efficiency, but greatly increases the efficiency.

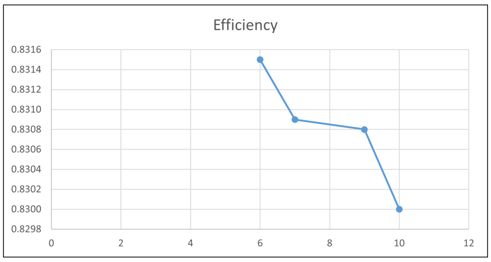

Figure 4.11: Efficiency Variation

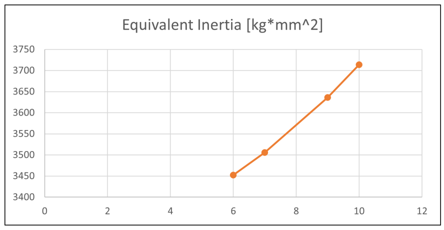

Figure 4.12: Equivalent Inertia Variation

4.1.7 Sensitivity Review

The effectiveness of each parameter is listed in Table 4.1. The effectiveness is based on how much of a variation in these parameters effects the efficiency and equivalent inertia. The last two parameters opposite correlations and thus it would be counter productive to modify these parameters for better results. The first three better have both positive correlations and have the strongest influence in descending order.

Variable	**Equivalent Inertia Correlation**	**Efficiency Correlation**	**Effectiveness**
Output Pin Centre Radius	Positive	Positive	1
Output Pin Radius	Positive	Positive	2
Housing Roller Radius	Positive	Positive	3
Modification Factor	Positive	Negative	4
Base Circle	Positive	Negative	5

Table 4.1

4.2 Genetic Algorithm

The genetic algorithm follows the basic backbone of biological evolution as expressed in Figure 4.14. It is comprised of a hierarchy; generation, population, parents, children and genes. It must be stated priori that the genetic algorithm cannot determine a global optimum, but rather a local optimum.

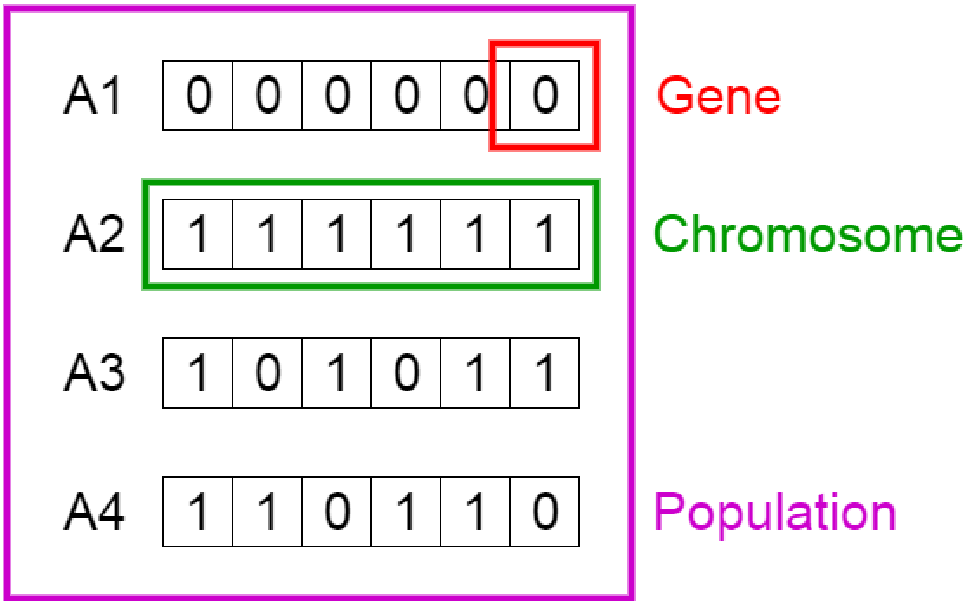

Figure 4.13: Genetic algorithm hierarchy[19]

It initially starts with the first generation that sparks a series of populations which is used in the model and produces an overall score related to the fitness function using each respective population. Each population is one of the parameters which is encoded in the binary form.

Afterwards there are three ways to repopulate the next generation:

- Mutation
- Selection
- Crossover

After the last population of the generation is run, the next generation is created based on the populations with the highest normalized overall scores which become parents and produce the children which is going to become the first population of the next generation. This mode of population generation is called the selection method.

Crossover is when a predefined number of genes is switched in-between the populations. Lastly as the name suggestion the mutation is when a single gene is modified and switched.

When each population is created it must satisfy the constraints provided to the optimiser, if it does not conform to the constraints then it is discarded and a new population is created again until it is acceptable.

Several criteria exist for the end condition for the optimisation such as:

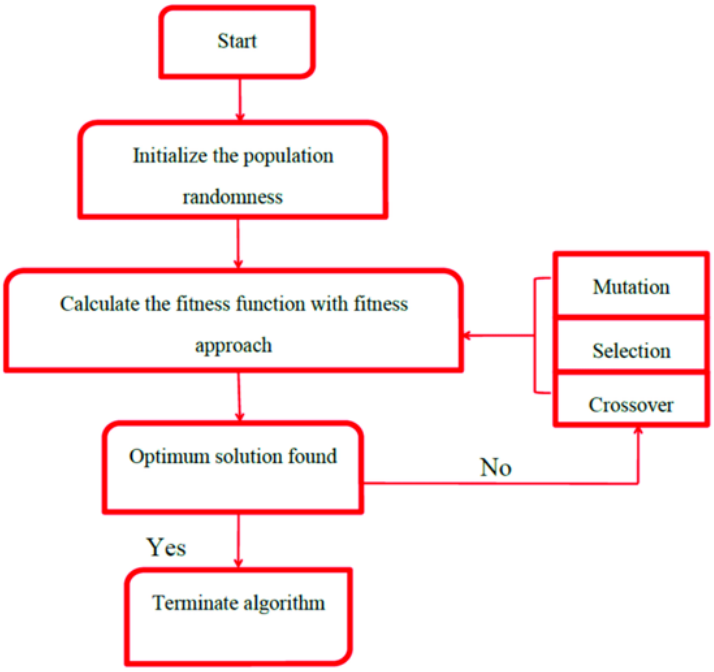

Figure 4.14: Block diagram for genetic algorithm[20]

4.3 Constraints

Constraints must be respected throughout the entire optimisation as a form of guideline to follow. In this particular case the constraints are presented to the genetic algorithm in the form of linear system comprised of a matrix, a vector comprised of the free variables and a resulting vector of known terms like in Equation 4.2.

$$\begin{aligned} Ax &<= b \\ A_{eq}x &= b_{eq} \end{aligned} \tag{4.2}$$

The equation above reflects the linear constraints because. The vector "x" contains is a vector of length of number of free variables, which contains the population for that generation. The matrix "A" has a number of rows equal to number of constraints and number of columns equal to the number of free variables. The vector "b" contains all the known terms regarding the constraint formulation.

However due to the complex nature of the problem almost all of the constraints are complex in nature, but this requires a separate file because the constraints are a function of the free variables. Both the complex equalities and inequalities must be rewritten in the form in Equation 4.3.

$$\begin{aligned} c(x) &= 0 \\ c_{eq}(x) &<= 0 \end{aligned} \tag{4.3}$$

There are **five** constraints the optimisation must follow.

1. Housing roller interference ⇒ Avoid overlapping of the housing roller
2. Output pin hole interference ⇒ Avoid overlapping of the output pin hole interference
3. Output pin hole and Input shaft interference ⇒ The output pin hole should not interfere with the input shaft
4. Output pin hole circle and cycloidal profile ⇒ The circle for the output pin holes does not reach the cycloidal profile
5. Housing case radius and housing roller circle ⇒ Make sure the housing roller circle is within the housing limits

The Figures 4.15, 4.16 and 4.17 represent examples of the type of constraints related to the optimisation such as the first, fourth and third respectively to the figures.

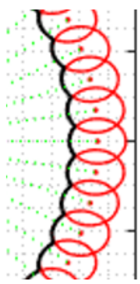

Figure 4.15: Example of a geometric constraint involving the housing rollers

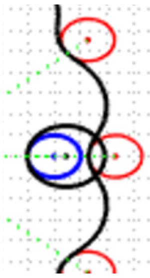

Figure 4.16: Example of a geometric constraint involving the output pins

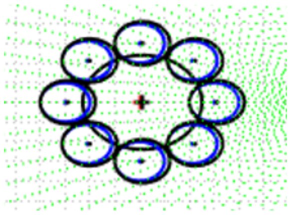

Figure 4.17: Example of a geometric constraint involving the input shaft

The vector x containing the free variables has the following order to its components:

$$x = [R_p, R_r, R_{pin}, R_{po}, x_{mod}] \tag{4.4}$$

4.3.1 Housing Roller Constraints

There are two constraints related to the housing roller radius. Firstly the interference amongst other rollers and that the housing roller circle doesn't exceed the housing radius.

The equation related to the housing roller interference is present in Equation 4.5. This relationship is the final expression that is obtained by simply writing the desired gap(δ) in terms of all of the geometric dimensions in the figure.

$$c(1) = 2R_r - OA_2 sin(\frac{2\pi}{N_{pr}}) < 0 \tag{4.5}$$

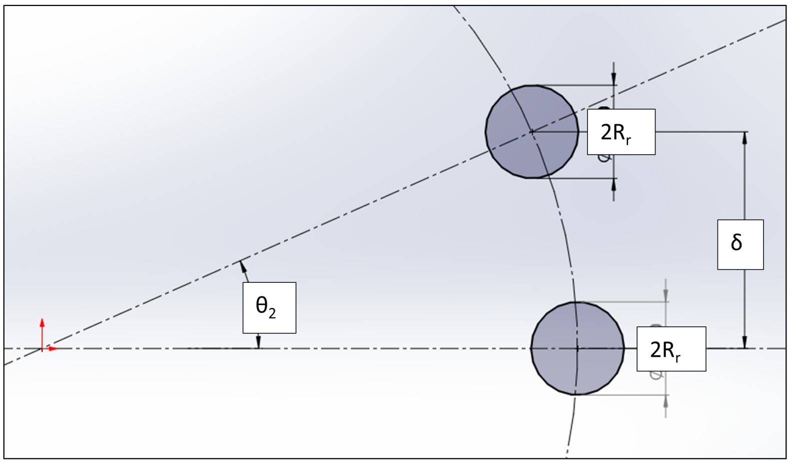

Figure 4.18

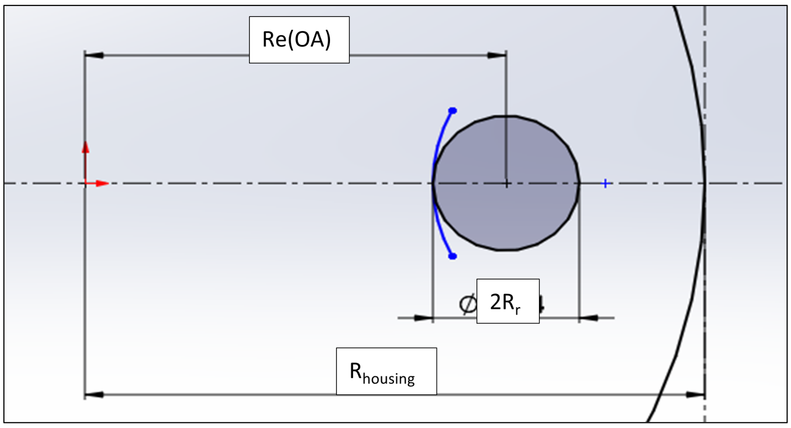

Figure 4.19

The second constraint involves making sure that the circle for the housing rollers does not exceed the radius of the housing.

$$c(2) = \Re(OA_1) - R_{housing} < 0 \tag{4.6}$$

4.3.2 Output Pin Constraints

The output pins have to satisfy the two similar constraints, as those previously stated in the housing roller constraints section.

The desired gap(δ) is written in term of the other geometry quantities in the figure below to obtain the equation below.

$$c(3) = 2R_h - \Im(OS_2) < 0 \tag{4.7}$$

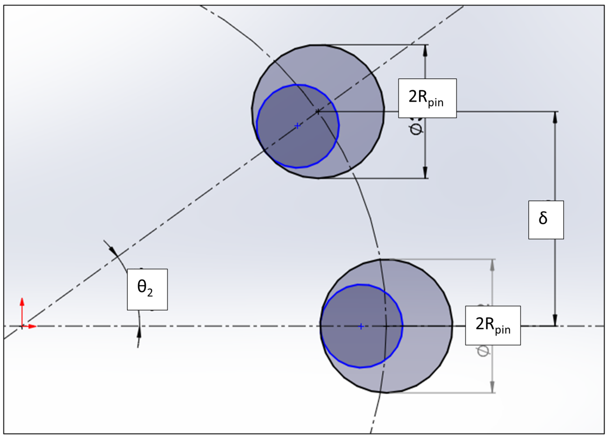

Figure 4.20

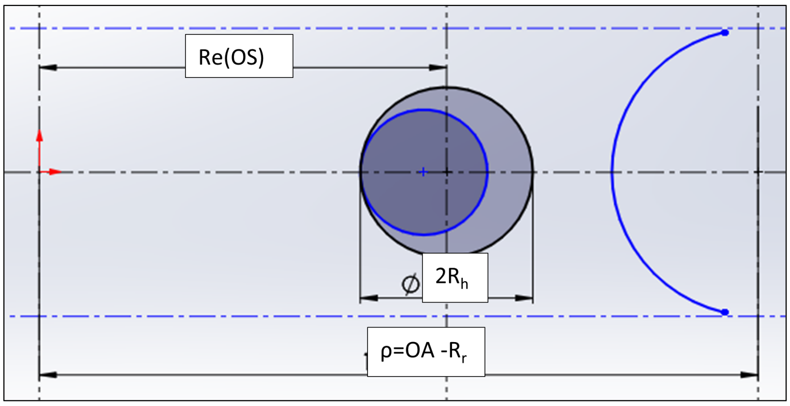

Figure 4.21

For the interference of the output pin hole with the cycloidal drive profile is given by the relationship below.

$$c(4) = (\Re(OS_1) + R_h) - (\Re(OA_1) - R_r) < 0 \tag{4.8}$$

4.3.3 Input Shaft Constraints

The hole for the output pin hole should penetrate the input shaft nor should it be very close to the input shaft as it can lead to a weakening with the material strength.

$$c(5) = (1.1R_{shaft} + R_h) - \Re(OS_1) < 0 \tag{4.9}$$

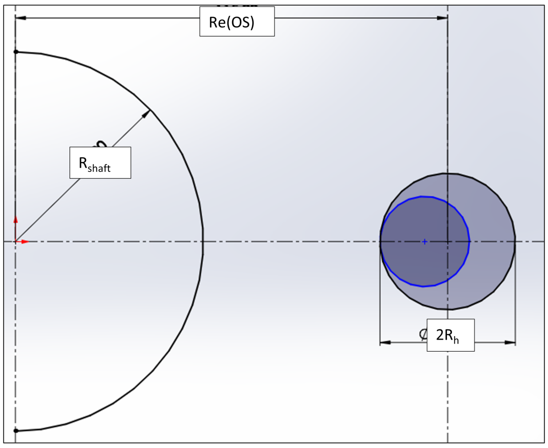

Figure 4.22

4.4 Pareto Front

The end result of the optimisation can be summed up in the form of a Pareto Front diagram like the Figure 4.23. The pareto front defines a line between the feasible and infeasible zones, on each axis is denoted by the two objective function. On the diagram each population corresponds to a point and tends to outline the pareto front. The pareto front symbolically represents the line where there is no advantage to move in each direction of the other objective functions.

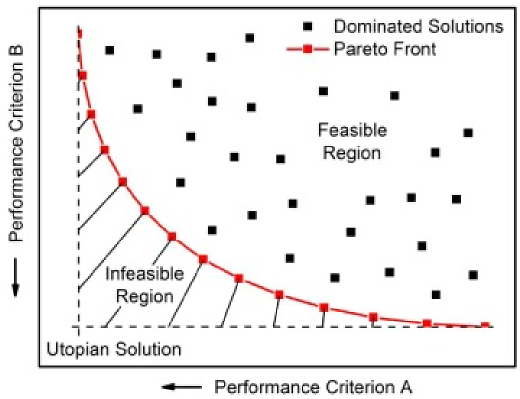

Figure 4.23: Pareto front[21]

Notice that in this case the efficiency is report with negative values this is because the Matlab gamultiobj function **minimises both** objective functions so in order to maximum the efficiency its sign must be inverted as shown in Figure 4.24.

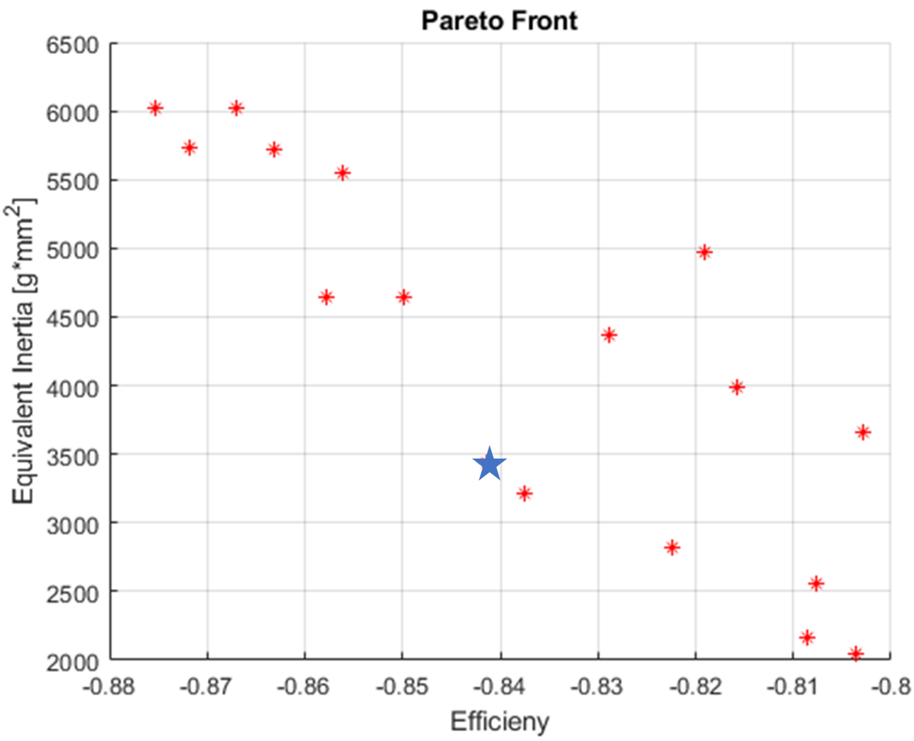

Figure 4.24: Pareto front

The optimal point is found is at (highlighted by the star in Figure 4.24):

Efficiency	0.8413	
Equivalent Inertia	3432.54	gmm^2

Based on the pareto front above the optimised parameters are:

Variable	Symbol	Value	Unit
Housing Roller Radius	R_r	1.20	mm
Output Roller Radius	R_{pin}	5.30	mm
Output Pin Circle Radius	R_{po}	24.40	mm
Housing Pin Circle Radius	R_p	37.60	mm
Modification Factor	x_{mod}	0.4296	mm

Other operating criteria:

Friction Coefficient		
Description	Symbol	Value
Disk-Roller Friction	μ_p	0.004
Disk-Pin Friction	μ_q	0.004
Input Bearing Friction	μ_{fsp}	0.004

Material	Steel, AISI 52100, 100Cr6, 1.3505
Disk Thickness	5 mm
Input Torque	455 Nm
Shaft radius	15 mm

Chapter 5

CAD Model

5.1 Housing Case

A CAD model was created to ensure that the not only the basic components would not cause any unforeseen issues, but also auxiliary components such as bearings, casing cases and snap rings. Notice that the configuration of the drive below matches the choice made above with regards to the bearing location as discussed in configuration section. The housing shape is defined by the layout of the drives' principle components such as the input shaft, output shaft, and the cycloidal disks mainly. In following sections the dimensions for each of the sub-components of the assembly have been reported.

Figure 5.1a shows the isometric view of the entire assembly while Figure 5.1b shows the section view of the assembly. The overall dimensions of the assembly have also been reported in Figure 5.2.

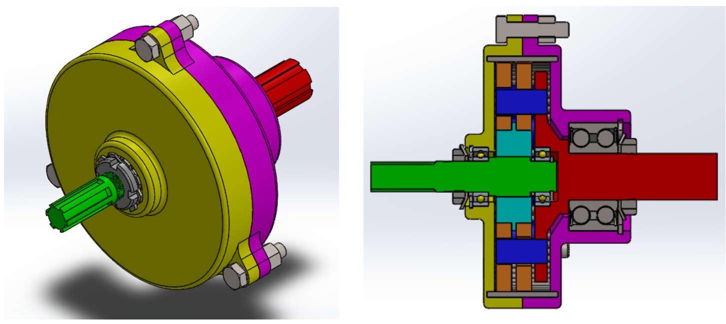

(a) Isometric view of the model

(b) Section view of the assembly from the right plane

Figure 5.1: CAD model of the drive assembly

Another consideration that must be stated is that some dimensions mainly referring to the input and output casing have been assigned arbitrarily such as the thickness of the casings, but this is can be easily verified by a simple FEM simulation of the casing. However if the casings were constructed by a rigid material such as cast iron or high strength aluminium alloys due to the ease of manufacturing then even a relatively thin case should be rigid enough to handle the normal operation of the gearbox, but the choice of thickness must still be verified nevertheless.

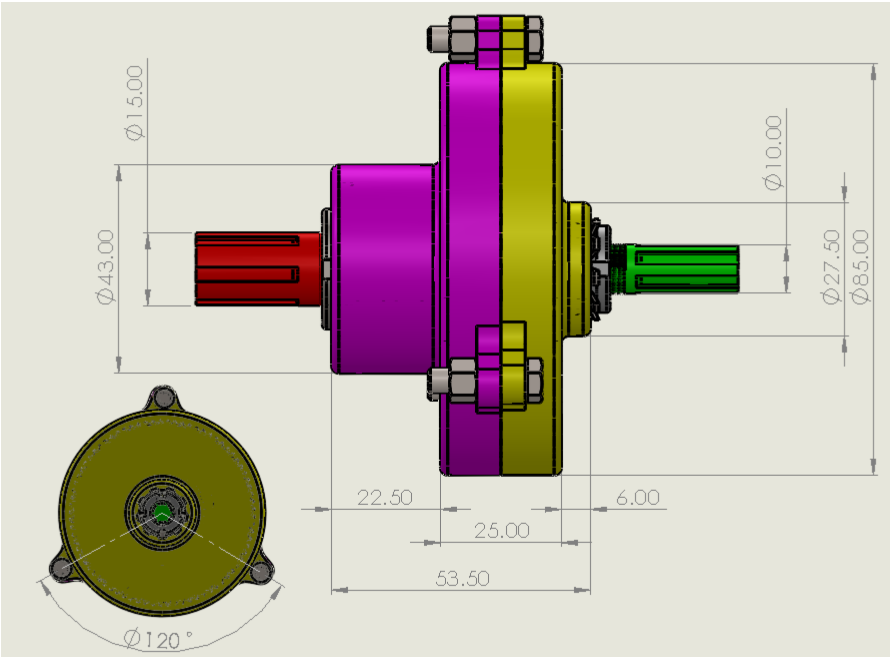

Figure 5.2: Overall dimensions of the assembly

The length of both the input and output shafts are based on the layout of the components and considering the splines which are needed to make mechanical connections with the gearbox.

Both the casing dimensions are reported in Figure 5.3 and 5.4 and due to there simple shape only the section view of half the component is reported.

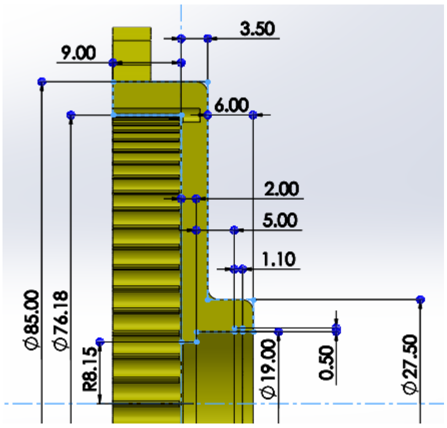

Figure 5.3: Overall dimensions of the input casing

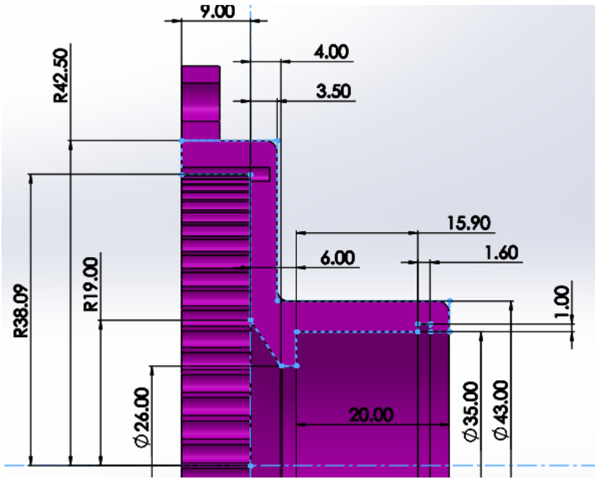

Figure 5.4: Overall dimensions of the output casing

5.2 Input and Output Shafts

In an effort to reduce the overall design of the gearbox instead of randomly assigning the diameter of the input and output shafts, they are sized based on their experienced loads, to which it comes out that only the input shaft can be resized from 15mm to 10mm, however the unfortunately the output shaft must remain at 15 mm. This was achieved by considering the bending and torsional stress seen by each shaft and based on its equivalent Von Mises stress to establish whether it satisfied an appropriate safety factor which in this case was 1.5. In the Figure 5.5 the loads experienced by both shafts can be seen in the free body diagram and subsequently their internal reactions are calculated.

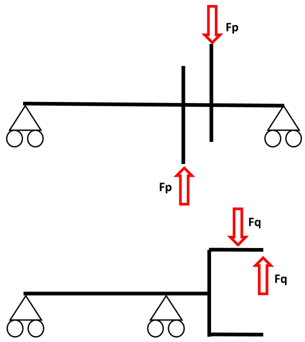

Figure 5.5: Free body diagram of input(left) and output(right) shafts

The equations expressed in the 3.46 expresses the equivalent Von Mises stress and section moduli for bending and torsion. In order to check whether the diameter satisfies the safety factor, the moduli are iterated through progressive sizes to check each respective safety factor against the pre-defined value. The Figures 5.6 and 5.7 shows the result of the safety factor of each shaft diameter. Although for any given diameter its respective safety factor seems like to be a straight line, this is due to the fact that there isn't much of a variation in the safety factor along the shafts length and coupled together with the scale of the vertical axis as well.

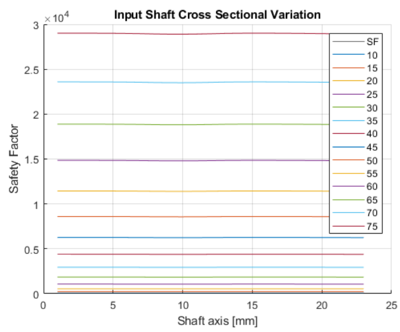

Figure 5.6: Safety factor along the length of the shaft for various diameters for the input shafts

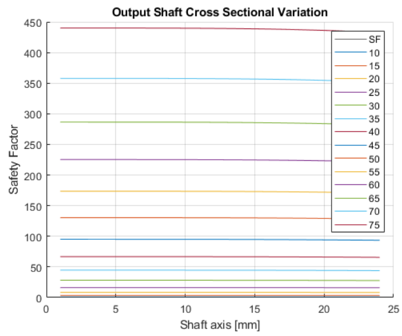

Figure 5.7: Safety factor along the length of the shaft for various diameters for the output shafts

Splines are also introduced on the shafts as a means to enable a stronger coupling for the shafts to other machines. The splines seen in Figure 5.2 are both internal splines cut into the shafts and follows **ISO 14-1982** standard, while the length of the spline is based on its ability to transmit power within safe limits as described by the set of equations in 5.1.

$$\sigma_c = \frac{TK_s}{ndLer} \tag{5.1}$$

Quantity	Unit	Description
r	mm	Mean radius of spline
n	-	Number of splines
Le	mm	Effective length of spline
T	Pa	Resulting shear stress
K_s	-	Service factor
σ_c	Pa	Resultant compressive stress
T	Pa	Resultant shear stress

Lastly the dimensions of the output shaft is reported in the figure below. An additional step is to re-enforce the connection of the disk to the shaft presents a significant source of stress concentration, this is done by placing a chamfer to avoid a sharp corner.

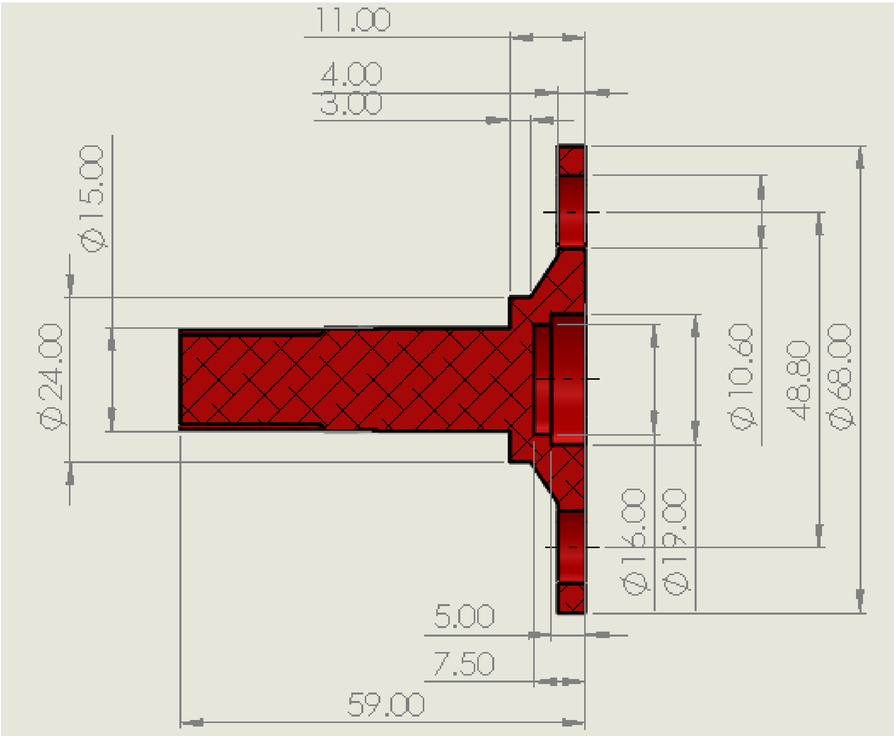

Figure 5.8: Overall dimensions of the output shaft

The bearings are held in place not only through interference fits, but also by means of snap rings and locknuts. The snap rings needed for both shafts follow the DIN 472 and DIN 471 for the external(DHO) and internal(DSH) rings respectively.

- Input Casing: DHO-19
- Input Shaft: DSH-10
- Outer Casing: DHO-35

The choice of a snap ring on the inner bearing for the input shaft as opposed to the use of a locknut is mainly due to the lack of space. As for the SKF rated locknuts and washers which are in use:

- Input Shaft: KM0 and MB0
- Output Shaft: KM2 and MB2

The overall dimension of the input shaft with both external and internal shafts are reported in the Figure 5.9.

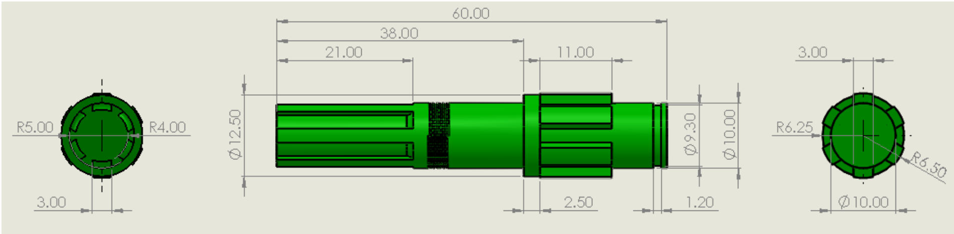

Figure 5.9: Overall dimensions of the input shaft

5.3 Cam

The most important component of the gearbox assembly is the cam located on the input shaft. The purpose of the cam is to introduce the eccentricity to the cycloidal disk, because the alternative was to machine the eccentricity onto the shaft which introduce another level of complexity. Another function of the cam is to provide the spacing required between the two disk, the reason why two disk was used was to avoid an asynchronous behaviour which will leads to heavy oscillations. Instead of relying on an interference fit between the cam and the input shaft an external spline has been introduced to offer better torque transmissiblility (likewise with the internal splines on the shaft ends, these spline also follow the previously mentioned ISO standard for splines). Another distinction is the space introduced between each disk to avoid any unwanted interactions between the two disks.

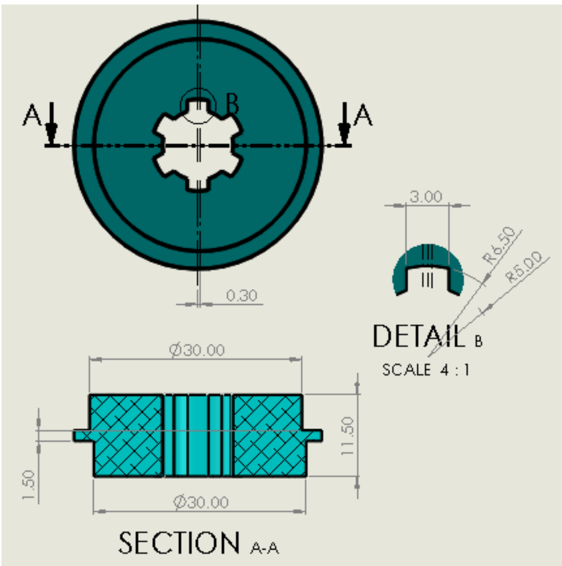

Figure 5.10: Overall dimensions of the cam

5.4 Mass and Equivalent Inertia

The material for other auxiliary components such as the shafts, housing casing, and the cam are machined in 6061 aluminium alloy, mainly due to is high strength to weight ratio in an effort to reduce the overall weight without compromising its structural integrity. The resulting design produces the following physical characteristics of the drive reported in Table 5.1. The equivalent inertia has significantly increases due to the presence of the other components as opposed equivalent inertia calculated in the optimisation section.

Dimension	Value	Unit
Length	53.5	mm
Diameter	85.0	mm
Mass	745	g
Equivalent Inertia	564175.63	gmm^2

Table 5.1: CAD Model physical characteristics

Chapter 6

Conclusion

In essence an initial hypothesis focused on an operating principle for a cycloidal gearbox which involved a linear mathematical model written in terms of a fixed reference frame. The next step, based on existing configurations available both commercially and in scientific journals was the selection of a suitable layout on the basis of its rigidity and compact size for this particular application.

After a working model was established and it is capable of providing key output parameters such as theoretical efficiency, output torque and input torque. Utilizing other literature sources to compare the output parameters to ensure the model was working as expected before moving onto the optimisation phase.

Optimisation was carried out successfully by means of a matlab genetic algorithm called the "gamultiobj". Five major geometric parameters are optimised, these parameters influence the overall operation of the gearbox. The model was altered slightly to cater to the optimisers' requirements and to respect the geometrical constraints of the problem. The geometric constraints were presented separately to the solver in the form of non-linear constraints. The optimiser minimises two objectives; efficiency and equivalent inertia. The simulation although time consuming with a duration of roughly five hours produced an acceptable pareto front and an optimal operating point within the provided geometric limits.

In addition to the optimal geometrical parameters a further step is considered by constructing the housing of the complete gearbox not only to check its feasibility but to have an idea of the overall dimensions of the gearbox along with its bearings. The required auxiliary components for the gearbox were sized and selected based on the operating conditions, resulting in a highly light weight and efficient gearbox ready for production.

A further consideration could be to study the behaviour of the non-linear model of the gearbox. Due the elasticity nature of material some form of deformation is expected and the can translated into a form of a stiffness force, however due to the complex nature of all the types of contacts, such as the contact between the housing roller and the cycloidal disk and the output pins and the cycloidal disk. The overall stiffness force can be characterized with a non-linear stiffness force, furthermore the non-linearity section of the force is expressed by the fact that the stiffness force is elevated to a positive exponent. Non-linear models tend to show a more realistic result because in reality the imposed output load on the gearbox drastically effects the experimental efficiency over its entire operating range. Another side of the non-linear model is that it is a time dependent dynamic problem in most cases thus further increasing the computation time for the optimisation. It requires the solving of a dynamic problem and a differential equation together.

Experiments done in a laboratory situation to record for a given cycloidal gearbox the efficiency, can support the non-linear model because by calculating the theoretical efficiency and measuring the experimental efficiency the non-linear model can be calibrated.

Chapter 7

Appendix A: Kennedy Theorem

When several bodies are in motion at any given instant there is a point which is characterised by being stationary, in other words at that point the velocity is null, this is called the instantaneous center of rotation (ICR). The basis for Kennedy theorem is as follows, if three bodies have plane motion relative to one another, then there are three instant centers, and the three instant centers all lie on the same line.

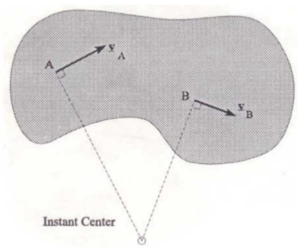

Figure 7.1: Example of a solid body in motion[22]

For each body in motion simple take a two different and independent points and draw the velocity vector for each point. Based on the velocity vectors the points can be used to identify the instantaneous center of rotation like that in Figure 7.1. The same principle applies for multi-linkage bodies like that in Figure 7.2.

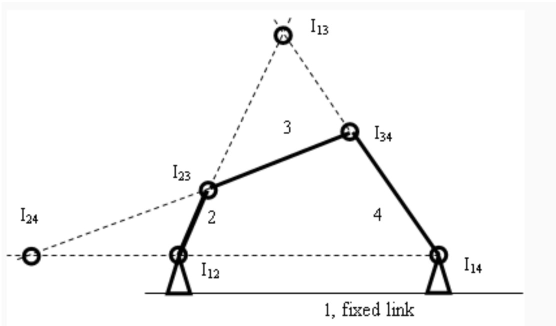

Figure 7.2: Example of a multi-linkage body in motion[23]

Chapter 8

Appendix B: Bearing Life Verification

The objective of the overall design is to make the entire assembly light and seem less bulky therefore the selection was initially made primarily on the smallest possible bearing size for each respective shaft. The obvious choice of type of bearing was the **deep grove ball bearing** due to the its size like in Figure 8.1a, but also mainly since the overall load experienced is radial therefore not requiring axial bearings. Moreover in the unlikely case that the bearing must handle an axial load the chosen bearings are more than capable of handling a limited axial load.

(a) Example of deep grove ball bearing[24]

(b) Example of double row ball bearing[25]

However size is not the the only selection criteria, the other being the bearing arrangement. The essence of the selection is to be able to locate the bearing axially in the likely event of thermal expansion during operation which can be mitigated by utilizing not only appropriate bearings but also placing them in a suitable location within the machine structure. It is for this reason that the SKF 3202 double row ball bearing was selected along with the SKF 61800 bearing to provide a locating bearing and non locating bearing respectively.

The bearing selection for the input shaft and the output shaft:

- Input Shaft ⇒ SKF 61800
- Output Shaft ⇒ SKF 3202 and SKF 61800

In Figure 8.2 the bearing on the left hand side acts as the locating bearing while the right hand bearing serves the purpose of the non-locating bearing.

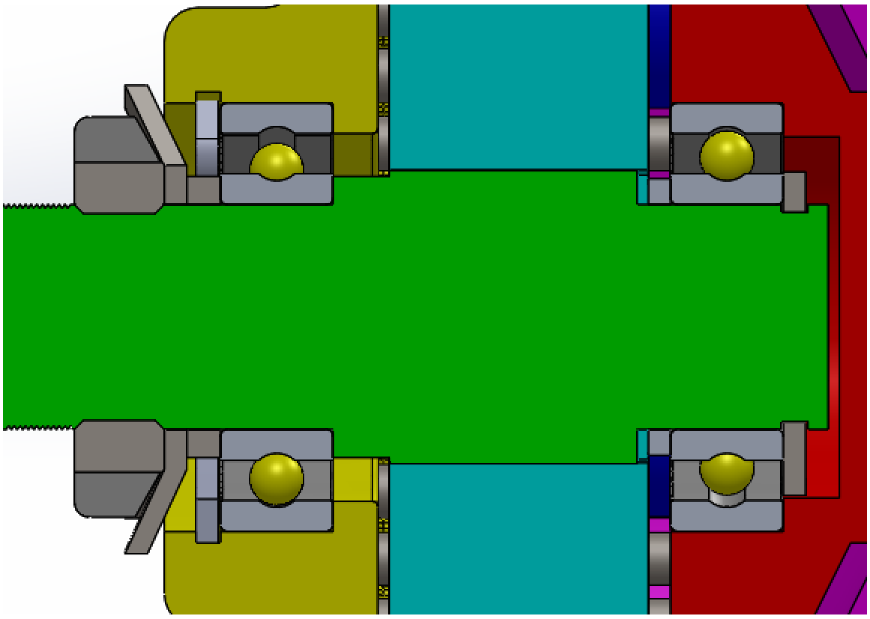

Figure 8.2: Input shaft bearing arrangement

In Figure 8.3 the bearing on the right hand side acts as the locating bearing while the left bearing serves the purpose of the non-locating bearing.

An important distinguish to be highlighted is the fact that the non-locating bearing for both shafts act as a common bearing.

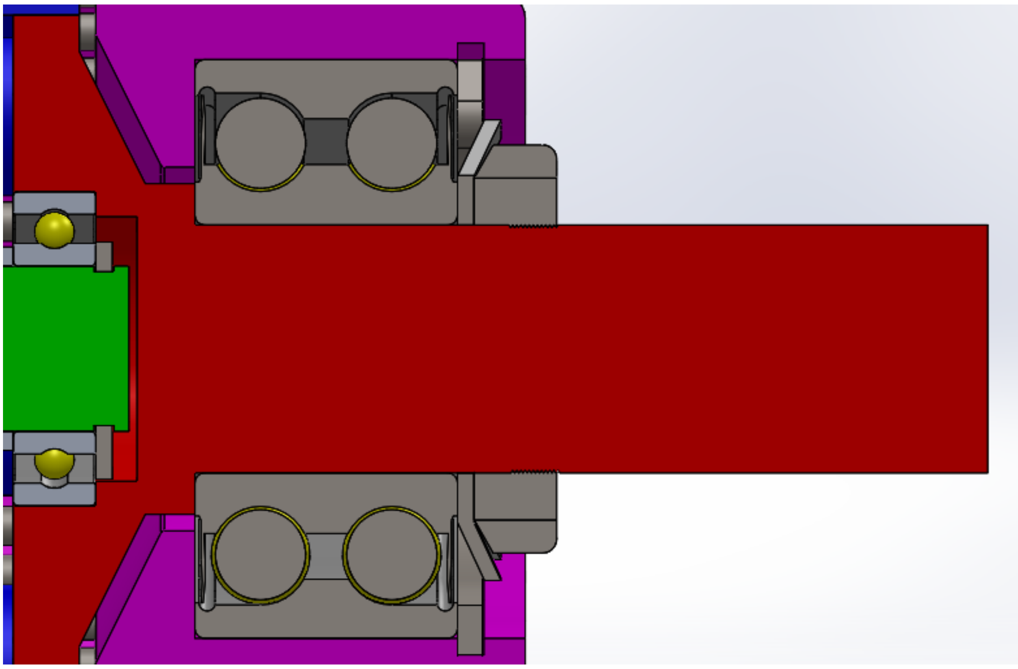

Figure 8.3: Output shaft bearing arrangement

The choice of bearing series is usually based on several factors such as: (In the occasion where no information regarding the respective bearing selection factor is mentioned then the worst case has been assumed.)

- Lubricant
- Operating temperature
- Contamination level
- Rotational speed
- Bearing mean diameter
- Fatigue limit
- Dynamic load rating
- Equivalent load

Assuming these parameters are the same for both bearings:

Operating Temperature [$^\circ$ C]	40
Contamination Level	0.1

The reaction force experienced by the bearings can be considered as a constant magnitude force that simply rotates around a fixed axis. Likewise the magnitude of this force depends on the external force and moments acting on the shafts, this too also rotates around a fixed axis.

The procedure for the determination of the bearing life in terms of millions of cycles is given by Equation 8.1 provided by SKF.

$$L_{10} = a_1 a_{SKF} \left(\frac{C}{P}\right)^p \tag{8.1}$$

Each factor a_1 and a_{SKF} are multipliers that modify the life expectancy of the bearing according to its environment and operating conditions.

The reliability factor (a_1) is based on the probability of failure of the bearing and it usually one, which corresponds to a 10% chance of failure.

The SKF life modification factor (a_{SKF}) is based on both the operating conditions and environment as follows. Utilizing the mean diameter of the bearing and rotational speed in Figure 8.4, it provides the actual viscosity. Then once an appropriate lubricant is chosen the rated viscosity, in Figure 8.5 and viscosity ratio, in Equation 8.2, can be obtained. Finally using the non-dimensional parameter (Equation 8.3), coupled together with the Figure 8.6 the SKF factor is achieved.

$$\kappa = \frac{\nu}{\nu_1} \tag{8.2}$$

$$Non - dimensional\, parameter \Rightarrow \eta_c \frac{P_u}{P} \tag{8.3}$$

It is worth noting that in the next section two different lubricants have been proposed one for each bearing, however it is impractical thus it's advisable to use the lower of the two suggested lubricants.

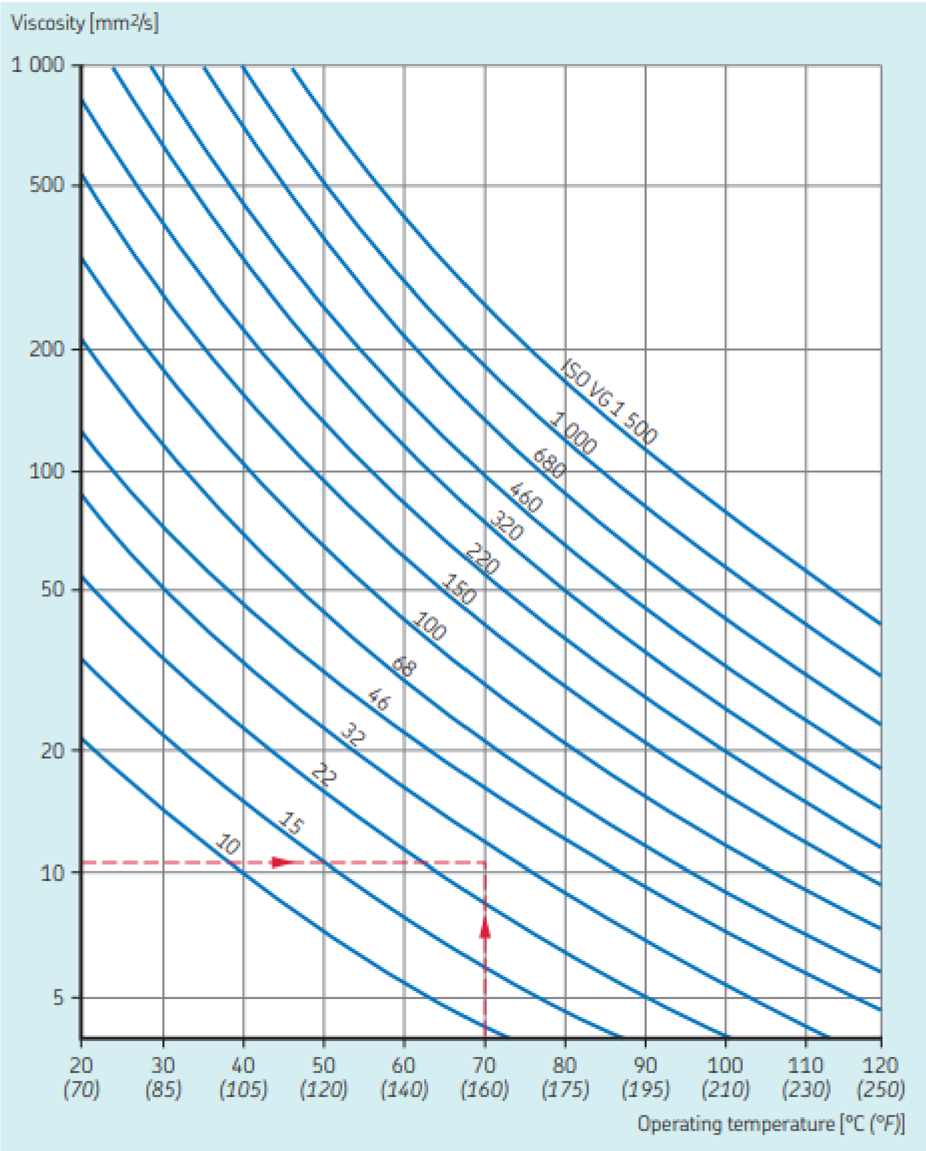

Figure 8.4: Actual viscosity graph[26]

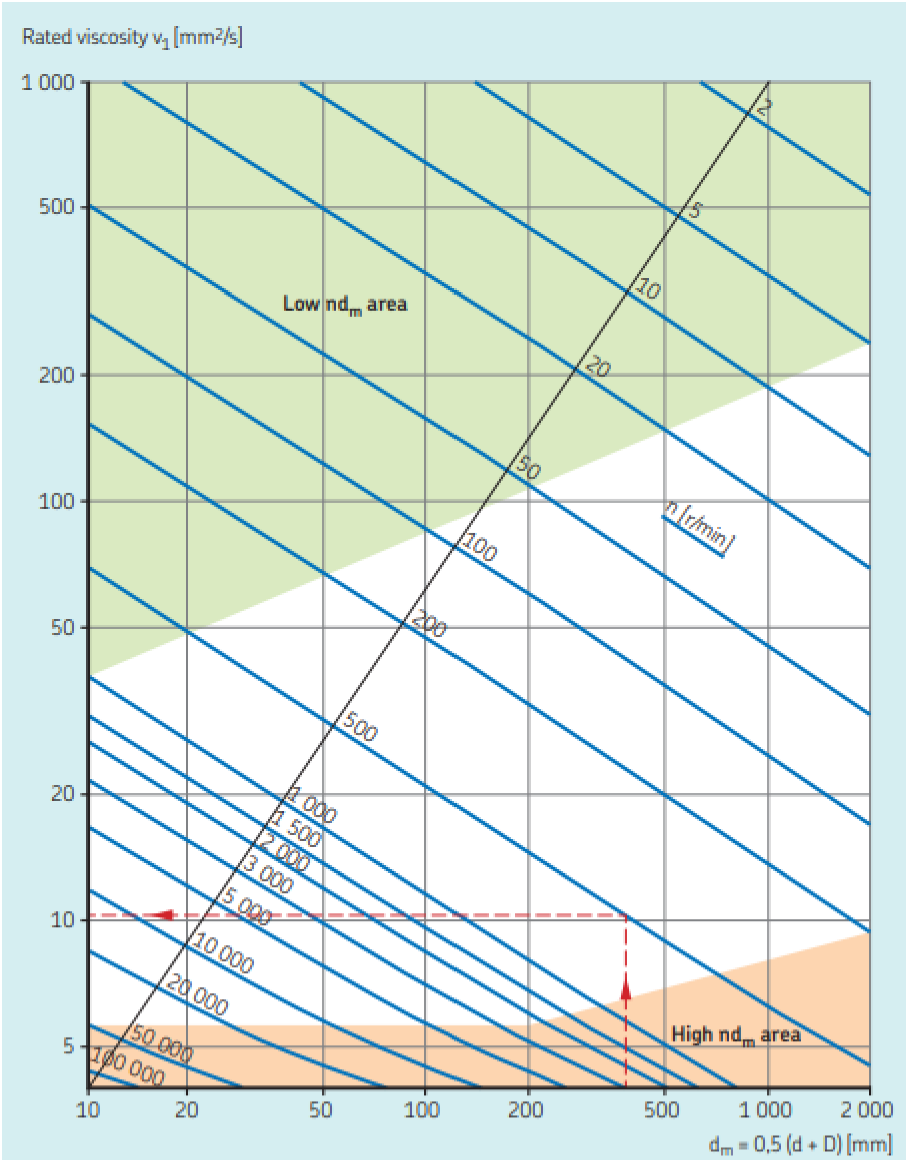

Figure 8.5: Rated viscosity graph[26]

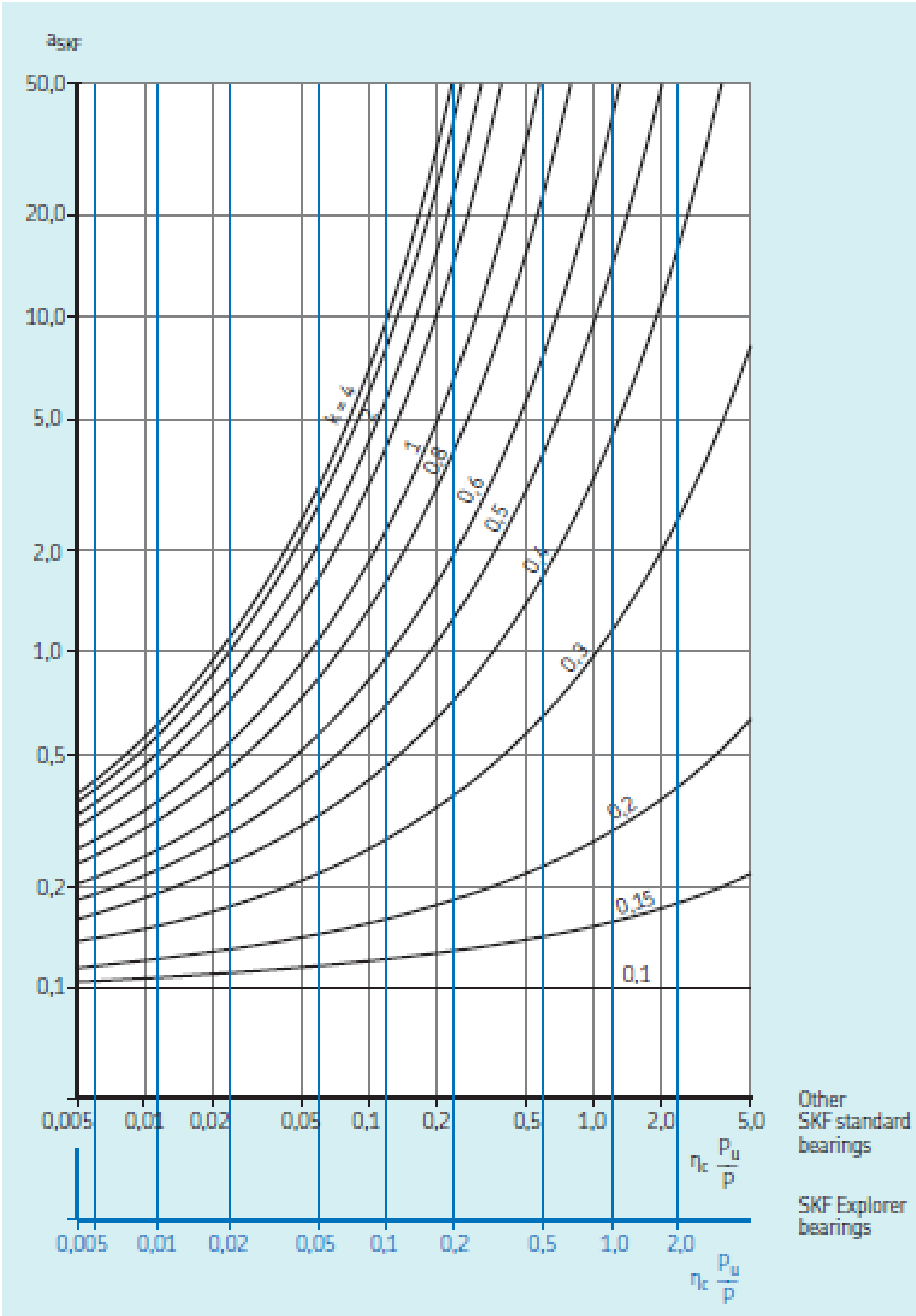

Figure 8.6: a_{SKF} coefficient for radial ball bearings[26]

8.0.1 SKF 61800 Verification

Technical specification

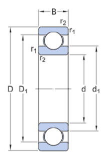

DIMENSIONS

d	10 mm	Bore diameter
D	19 mm	Outside diameter
B	5 mm	Width
d1	≈12.74 mm	Shoulder diameter
D1	≈16.26 mm	Shoulder diameter
r1,2	min.0.3 mm	Chamfer dimension

CALCULATION DATA

Basic dynamic load rating	C	1.72 kN
Basic static load rating	C_0	0.83 kN
Fatigue load limit	P_u	0.036 kN
Reference speed		80 000 r/min
Limiting speed		48 000 r/min
Minimum load factor	k_r	0.015
Calculation factor	f_0	14.8

Figure 8.7: Bearing dimensions and technical data[27]

The values for each of the parameters described in the section above are reported in the table below.

Quantity	Symbol	Value	Unit
Mean Diameter	d_{mean}	14.5	mm
Rotational Speed	n_{rot}	1000	rpm
Contamination Level	η_c	0.1	
Exponent	p	3	
ISO VG Lubricant		32	
Operating Temperature		40	$°C$
Rated Viscosity	ν_1	35	$\frac{mm^2}{s}$
Actual Viscosity	ν	40	$\frac{mm^2}{s}$
Equivalent Dynamic Load	P	0.0011	kN
Reliability Factor	a_1	1	
Viscosity Ratio	κ	1.143	
SKF Life Modification Factor	a_{SKF}	50	
Life in Millions of Cycle	L_{10}	2.18E+11	millions of cycles
Life in Operating Hours	L_{hours}	3.64E+12	hours of cycles

8.0.2 SKF 3202 Verification

Technical specification

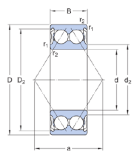

DIMENSIONS

d	15 mm	Bore diameter
D	35 mm	Outside diameter
B	15.9 mm	Width
d2	≈20.2 mm	Recess diameter inner ring shoulder
D2	≈30.7 mm	Recess diameter outer ring shoulder
r1,2	min.0.6 mm	Chamfer dimension inner ring
a	21 mm	Distance pressure point(s)

CALCULATION DATA

Basic dynamic load rating	C	11.2 kN
Basic static load rating	C_0	6.8 kN
Fatigue load limit	P_u	0.285 kN
Reference speed		22 000 r/min
Limiting speed		18 000 r/min
Calculation factor	k_r	0.06
Calculation factor	e	0.8
Calculation factor	X	0.63
Calculation factor	Y_0	0.66
Calculation factor	Y_1	0.78
Calculation factor	Y_2	1.24

Figure 8.8: Bearing dimensions and technical data[28]

The values for each of the parameters described in the section above are reported in the table below.

Quantity	Symbol	Value	Unit
Mean Diameter	d_{mean}	25	mm
Rotational Speed	n_{rot}	12.99	rpm
Contamination Level	η_c	0.1	
Exponent	p	3	
ISO VG Lubricant		10	
Operating Temperature		40	$°C$
Rated Viscosity	ν_1	8	$\frac{mm^2}{s}$
Actual Viscosity	ν	10	$\frac{mm^2}{s}$
Equivalent Dynamic Load	P	0.0034	kN
Reliability Factor	a_1	1	
Viscosity Ratio	κ	1.25	
SKF Life Modification Factor	a_{SKF}	50	
Life in Millions of Cycle	L_{10}	2.00E+12	millions of cycles
Life in Operating Hours	L_{hours}	2.24E+15	hours of cycles

Bibliography

[1] R. Galluzzi et al. "Rotary regenerative shock absorbers for automotive suspensions". In: *Mechatronics* 77.1 (2021), pp. 1–12. DOI: https://doi.org/10.1115/1.4044456.

[2] C. Zhang et al. *Integration of regenerative shock absorber into vehicle electric system*. 2014. URL: https://www.spiedigitallibrary.org/conference-proceedings-of-spie/9057/1/Integration-of-regenerative-shock-absorber-into-vehicle-electric-system/10.1117/12.2045189.short?SSO=1.

[3] Y.R. Yong et al. *Simulation on Eddy Current Damper and Its Regenerative Behaviour in Shock Absorber for Electric Vehicle*. 2013. URL: https://www.spiedigitallibrary.org/conference-proceedings-of-spie/9057/1/Integration-of-regenerative-shock-absorber-into-vehicle-electric-system/10.1117/12.2045189.short?SSO=1.

[4] Britannica. *Harmonic Drive*. 2021. URL: https://www.britannica.com/technology/Harmonic-Drive.

[5] MathWorks. *Cycloidal Drive*. 2021. URL: https://it.mathworks.com/help/physmod/sdl/ref/cycloidaldrive.html.

[6] tec-science. *How does a cycloidal drive work?* 2019. URL: https://www.tec-science.com/mechanical-power-transmission/planetary-gear/how-does-a-cycloidal-gear-drive-work/.

[7] Transckyo. *Reducers/Gearboxes*. -. URL: https://transcyko.com/static/2a766e5ac1b56623fb90624d257a3091/202011-TS-EN.pdf.

[8] Sumitomo Drive Technologies. *Cyclo Drive 6000 Reducer*. -. URL: https://emeia.sumitomodrive.com/en-de/product/cyclo-drive-6000-reducer.

[9] ESA Eppinger GmbH. *CT Cycloid Gearboxes*. 2021. URL: https://www.eppinger%20gears.com/downloads/kataloge/eppinger_catalogue_ct%20cycloid%20gearboxes_en.pdf.

[10] Nabtesco. *RV series*. 2021. URL: https://www.nabtescomotioncontrol.com/pdfs/RVseriesENG_051110.pdf.

[11] Spinea. *TwinSpin*. 2021. URL: https://www.spinea.com/en/products/twinspin/t-series.

[12] M.Blagojevic et al. *Numerical and experimental analysis of the cycloid disc stress state*. 2014. URL: https://www.researchgate.net/figure/D-model-of-the-investigated-single-stage-cycloidal-speed-reducer_fg3_262106089.

[13] Myung-Seop Lim and Chung-Seong Lee. *Tolerance-Insensitive Design of the Magnet Shape for a Surface Permanent Magnet Synchronous Motor*. 2020. URL: https://www.mdpi.com/1996-1073/13/6/1311/htm.

[14] J.G. Blanche et al. "Cycloid Drives With Machining Tolerances". In: *Journal of Mechanical Design* 111.3 (1989), pp. 337–344. DOI: https://asmedigitalcollection.asme.org/mechanicaldesign/article-abstract/111/3/337/420932/Cycloid-Drives-With-Machining-Tolerances?redirectedFrom=fulltext.

[15] P.Davoli et al. "Theoretical and Experimental Analysis of a Cycloidal Speed Reducer". In: *ASME. J. Mech. Des.* 130.11 (2008), pp. -. DOI: https://doi.org/10.1115/1.2978342.

[16] Jean-Luc Dion et al. "Theoretical and Experimental Study for An Improved Cycloid Drive Model". In: *ASME. J. Mech. Des.* 87.1 (2019), pp. -. DOI: https://doi.org/10.1115/1.4044456.

[17] Christian Firrone. *Powerpoint slide for hertzian contact, Machine Design, Politecnico di Torino*. URL: -.

[18] Amesweb. *Hertzian Contact Stress Calculator*. 2021. URL: https://amesweb.info/HertzianContact/HertzianContact.aspx.

[19] Vijini Mallawaarachchi. *Introduction to Genetic Algorithms — Including Example Code*. 2017. URL: https://towardsdatascience.com/introduction-to-genetic-algorithms-including-example-code-e396e98d8bf3.

[20] Wenqian Ruan et al and Xuedan Shi. *Modeling of Malachite Green Removal from Aqueous Solutions by Nanoscale Zerovalent Zinc Using Artificial Neural Network*. 2017. URL: https://www.researchgate.net/publication/321985815_Modeling_of_Malachite_Green_Removal_from_Aqueous_Solutions_by_Nanoscale_Zerovalent_Zinc_Using_Artificial_Neural_Network/citation/download.

[21] Artur Schweidtmann et al and Adam Clayton. "Machine learning meets continuous flow chemistry: Automated optimization towards the Pareto front of multiple objectives," in: *ASME. J. Mech. Des.* 352.1 (2018), pp. 227–282. DOI: `https://doi.org/10.1016/j.cej.2018.07.031.`.

[22] Norton. *EMCH 332 Kinematics,* -. URL: `http://www.me.sc.edu/fs/rochelea/EMCH-332/handout04.pdf`.

[23] Shiksha. *Module 3. Velocity and Acceleration Analysis,* 2014. URL: `http://ecoursesonline.iasri.res.in/mod/page/view.php?id=125550`.

[24] SKF. *Deep groove ball bearings*. 2021. URL: `https://www.skf.com/group/products/rolling-bearings/ball-bearings/deep-groove-ball-bearings`.

[25] SKF. *Angular contact ball bearings, double row.* 2021. URL: `https://www.skf.com/group/products/rolling-bearings/ball-bearings/angular-contact-ball-bearings/double-row-angular-contact-ball-bearings/productid-3202%20A-2ZTN9%2FMT33`.

[26] SKF. *Roller bearings*. 2021. URL: `https://www.skf.com/binaries/pub12/Images/0901d196802809de-Rolling-bearings---17000_1-EN_tcm_12-121486.pdf`.

[27] SKF. *61800*. 2021. URL: `https://www.skf.com/group/products/rolling-bearings/ball-bearings/deep-groove-ball-bearings/productid-61800`.

[28] SKF. *3202*. 2021. URL: `https://www.skf.com/group/products/rolling-bearings/ball-bearings/angular-contact-ball-bearings/double-row-angular-contact-ball-bearings/productid-3202%20A-2ZTN9%2FMT33`.